

A Report On:

A High-Resolution Pressure-Based Algorithm for Fluid Flow at All Speeds

(SPC-99-4003)

Submitted to:

European Office of Aerospace Research and Development

(EOARD)

by

F. Moukalled[♥] and M. Darwish
American University of Beirut,
Faculty of Engineering & Architecture,
Mechanical Engineering Department,
P.O.Box 11-0236
Beirut - Lebanon

DISTRIBUTION STATEMENT A
Approved for Public Release
Distribution Unlimited

June 9, 1999

DTIC QUALITY INSPECTED 4

19990809 052

[♥]Corresponding author. Email: memouk@aub.edu.lb

AQF99-11-2003

REPORT DOCUMENTATION PAGE

Form Approved OMB No. 0704-0188

Public reporting burden for this collection of information is estimated to average 1 hour per response, including the time for reviewing instructions, searching existing data sources, gathering and maintaining the data needed, and completing and reviewing the collection of information. Send comments regarding this burden estimate or any other aspect of this collection of information, including suggestions for reducing this burden to Washington Headquarters Services, Directorate for Information Operations and Reports, 1215 Jefferson Davis Highway, Suite 1204, Arlington, VA 22202-4302, and to the Office of Management and Budget, Paperwork Reduction Project (0704-0188), Washington, DC 20503.

1. AGENCY USE ONLY (Leave blank)		2. REPORT DATE 9 June 1999	3. REPORT TYPE AND DATES COVERED Final Report	
4. TITLE AND SUBTITLE A High-Resolution Pressure-Based Algorithm for Fluid Flow at all Speeds			5. FUNDING NUMBERS F61775-99-WE003	
6. AUTHOR(S) Prof. Fadl Moukalled				
7. PERFORMING ORGANIZATION NAME(S) AND ADDRESS(ES) American University of Beirut ME Dept. PO Box: 11-0236 Beirut Lebanon			8. PERFORMING ORGANIZATION REPORT NUMBER N/A	
9. SPONSORING/MONITORING AGENCY NAME(S) AND ADDRESS(ES) EOARD PSC 802 BOX 14 FPO 09499-0200			10. SPONSORING/MONITORING AGENCY REPORT NUMBER SPC 99-4003	
11. SUPPLEMENTARY NOTES				
12a. DISTRIBUTION/AVAILABILITY STATEMENT Approved for public release; distribution is unlimited.			12b. DISTRIBUTION CODE A	
13. ABSTRACT (Maximum 200 words) This report results from a contract tasking American University of Beirut as follows: The contractor will formulate a High-Resolution Pressure-Based algorithm within a finite volume framework. He will develop a new unified pressure-based solution procedure equally valid at a wide range of Reynolds numbers (Mach=0.1 to 7) that is easy to implement and highly accurate. Further details are found in the proposal submitted on 20 Aug 1998.				
14. SUBJECT TERMS EOARD, Fluid Dynamics, Computational Fluid Dynamics (CFD)			15. NUMBER OF PAGES 76	
			16. PRICE CODE N/A	
17. SECURITY CLASSIFICATION OF REPORT UNCLASSIFIED	18. SECURITY CLASSIFICATION OF THIS PAGE UNCLASSIFIED	19. SECURITY CLASSIFICATION OF ABSTRACT UNCLASSIFIED	20. LIMITATION OF ABSTRACT UL	

NSN 7540-01-280-5500

Standard Form 298 (Rev. 2-89)
Prescribed by ANSI Std. Z39-18
298-102

ABSTRACT

A new collocated finite volume-based solution procedure for predicting viscous compressible and incompressible flows is presented. The technique is equally applicable in the subsonic, transonic, and supersonic regimes. Pressure is selected as a dependent variable in preference to density because changes in pressure are significant at all speeds as opposed to variations in density which become very small at low Mach numbers. The newly developed algorithm has two new features; (i) the use of the Normalized Variable and Space Formulation methodology to bound the convective fluxes; and (ii) the use of a high-resolution scheme in calculating interface density values to enhance the shock capturing property of the algorithm. The virtues of the newly developed method are demonstrated by solving a wide range of flows spanning the subsonic, transonic, and supersonic spectrum. Results obtained indicate higher accuracy when calculating interface density values using a High-Resolution scheme.

NOMENCLATURE

a_p^ϕ, a_E^ϕ	Coefficients in the discretized equation.
b_p^ϕ	Source term in the discretized equation for ϕ .
C_p	Coefficient equals to $1/RT$.
$D[\phi]$	The D operator.
$\hat{\mathbf{d}}_f$	Covariant unit vector (i.e. in the direction of \mathbf{d}_f).
$\mathbf{D}[\phi]$	The vector form of the D operator.
F_f	Convective flux at cell face 'f'.
f_f	Interpolation factor.
$H[\phi]$	The H operator.
$\mathbf{H}[\phi]$	The vector form of the H operator.
\mathbf{i}	Unit vector in the x-direction.
\mathbf{j}	Unit vector in the y-direction.
J_f^C	Total scalar flux across cell face 'f' due to convection.
J_f^D	Total scalar flux across cell face 'f' due to diffusion.
J_f	Total scalar flux across cell face 'f'.
M	Mach number
P	Pressure.
Q^ϕ	Source term for ϕ .
R	Gas constant.
\mathbf{S}_f	Surface vector.
$\hat{\mathbf{s}}_f$	Contravariant unit vector (i.e. in the direction of \mathbf{S}_f).

T	Temperature.
t	Time.
u, v	Velocity components in the x- and y- directions.
U_f	Interface flux velocity ($\mathbf{v}_f \cdot \mathbf{S}_f$).
\mathbf{v}	$u\mathbf{i} + v\mathbf{j}$.
x, y	Cartesian coordinates.
$\ a, b\ $	The maximum of a and b.

GREEK SYMBOLS

$\hat{\mathbf{e}}_f$	Space vector equal to $(\hat{\mathbf{n}}_f - \gamma \hat{\mathbf{d}}_f) \mathbf{S}_f$.
$\Delta[\phi]$	The Δ operator.
Φ	Dissipation term in energy equation.
Γ^ϕ	Diffusion for ϕ .
Ω	Cell volume.
α	Under-relaxation factor.
β	Thermal expansion coefficient also flow angle at inlet.
δt	Time step.
$\tilde{\phi}$	Normalized scalar variable.
ϕ	Scalar variable.
γ	Scaling factor also specific heat ratio.
μ	Viscosity.
ρ	Density.
∇	$\frac{\partial}{\partial x} \mathbf{i} + \frac{\partial}{\partial y} \mathbf{j} = \frac{\partial}{\partial \xi} \mathbf{g}^\xi + \frac{\partial}{\partial \eta} \mathbf{g}^\eta$

SUBSCRIPTS

- e, w, . Refers to the east, west, ... face of a control volume.
- E,W,.. Refers to the East, West, ... neighbors of the main grid point.
- f Refers to control volume face f.
- F Refers to main grid point F.
- NB Refers to neighbours of the P grid point.
- P Refers to the P grid point.

SUPERSCRIPTS

- \circ Refers to values from the previous time step.
- (n) Refers to value from the previous iteration.
- *
- ' Refers to correction field.
- C Refers to convection contribution.
- D Refers to diffusion contribution.
- DC Refers to cross diffusion.
- DN Refers to normal diffusion.
- HR Refers to values based on a HR scheme.
- U Refers to values based on the UPWIND scheme.
- x Refers to component in x-direction.
- y Refers to component in y-direction.
- ϕ Refers to dependent variable.

INTRODUCTION

In Computational Fluid Dynamics (CFD) a great research effort has been devoted to the development of accurate and efficient numerical algorithms suitable for solving flows in the various Reynolds and Mach number regimes.

The type of convection scheme to be used in a given application depends on the value of Reynolds number. For low Reynolds number flows, the central difference or hybrid scheme is adequate [1]. In dealing with flows of high Reynolds number, numerous discretization schemes for the convection term arising in the transport equations have been employed [2,3,4,5,6,7,8,9,10,11].

On the other hand, the Mach number value dictates the type of algorithm to be utilized in the solution procedure. These algorithms can be divided into two groups: density-based methods and pressure-based methods, with the former used for high Mach number flows, and the latter for low Mach number flows. In density-based methods, continuity is employed as an equation for density and pressure is obtained from an equation of state, while in pressure-based methods, continuity is utilized as a constraint on velocity and is combined with momentum to form a Poisson like equation for pressure. Each of these methods is appropriate for a specific range of Mach number values.

The ultimate goal, however, is to develop a unified algorithm capable of solving flow problems in the various Reynolds and Mach number regimes. To understand the difficulty associated with the design of such an algorithm, it is important to understand the role of pressure in a compressible fluid flow [12]. In the low Mach number limit where density becomes constant, the role of

pressure is to act on velocity through continuity so that conservation of mass is satisfied. Obviously, for low speed flows, the pressure gradient needed to drive the velocities through momentum conservation is of such magnitude that the density is not significantly affected and the flow can be considered nearly incompressible. Hence, density and pressure are very weakly related. As a result, the continuity equation is decoupled from the momentum equations and can no longer be considered as the equation for density. Rather, it acts as a constraint on the velocity field. Thus, for a sequential solution of the equations, it is necessary to devise a mechanism to couple the continuity and momentum equations through the pressure field. In the hypersonic limit where variations in velocity become relatively small as compared to the velocity itself, the changes in pressure do significantly affect density. In this limit, the pressure can be viewed to act on density alone through the equation of state so that mass conservation is satisfied [12] and the continuity equation can be viewed as the equation for density. This view of the two limiting cases of compressible flow can be generalized in the following manner. In compressible flow situations, the pressure takes on a dual role to act on both density and velocity through the equation of state and momentum conservation, respectively, so that mass conservation is satisfied. For a subsonic flow, mass conservation is more readily satisfied by pressure influencing velocity than pressure influencing density. For a supersonic flow, mass conservation is more readily satisfied by pressure influencing density than pressure influencing velocity.

The above discussion highlights the difficulties associated with the use of density as a primary variable for computing low Mach number flows or mixed

compressible and incompressible flows. Most importantly, it reveals that for any numerical method to be capable of predicting both incompressible and compressible fluid flows the pressure should always be allowed to play its dual role and to act on both velocity and density to satisfy continuity. Hence, pressure methods developed for incompressible flow cannot be directly used for simulating flow at high Mach number without proper modifications. Furthermore, the behavior of pressure in compressible flow depends on Mach number. In the subsonic regime, it exhibits an elliptic behavior and the disturbances at any location affect and are affected by all neighboring points. In the supersonic regime, however, the behavior is hyperbolic and the value at a point depends on the data bounded by the characteristics passing through that point. The discretization scheme chosen for the pressure equation needs to model these features properly.

Several researchers [12,13,14,15,16,17,18,19,20,21,22,23] have worked on extending the range of pressure-based methods, with various degrees of success, to high Mach numbers following either a staggered grid approach [12-15] or a collocated variable formulation [16-23]. The method of Shyy and Chen [14], developed within a multigrid environment, uses a second-order upwind scheme in discretizing the convective terms. Moreover, at high Mach number values, a first order upwind scheme is employed for evaluating the density at the control volume faces. Yang et al [16] used a general strong conservation formulation of the momentum equations that allows several forms of the velocity components to be chosen as dependent variables. In the method developed by Marchi and Maliska [17], values for density, convection fluxes, and convection-

like terms at the control volume faces are calculated using the upwind scheme. Demirdzic et al [18], however, used a central difference scheme blended with the upwind scheme to evaluate these quantities. Lien and Leschziner [19,20] adopted the streamwise-directed density-retardation concept, which is controlled by Mach-number-dependent monitor functions, to account for the hyperbolic character of the conservation laws in the transonic and supersonic regimes. Politos and Giannakoglou [21] developed a pressure-based algorithm for high-speed turbomachinery flows following also the retarded density concept. In their method, unlike the work of Lien and Leschziner [19,20], the retarded density operates only on the velocity component correction during the pressure correction phase. Chen and Pletcher [22] developed a coupled modified strongly implicit procedure that uses the strong conservation forms of Navier-Stokes equations with primitive variables. The method of Karimian and Schneider [23] is formulated within a control-volume finite element framework. From the aforementioned literature review, it is obvious that in most of the published work the first order upwind scheme is used to interpolate for density when in the source of the pressure correction equation, exception being in the work presented in [18-21] where a central difference method is adopted. In the technique developed by Demirdzic et al [18], the second order central difference scheme blended with the upwind scheme is used. The blending relies on a factor varying between 0 and 1, which is problem dependent and has to be adjusted to eliminate oscillation or to promote convergence. In the work presented in [19-21], the retarded density concept is utilized in calculating the density at the control volume faces. This concept is based on factors that

are also problem dependent and requires the addition of some artificial dissipation to stabilize the algorithm (second-order terms were introduced), which complicate its use.

To this end, the objective of this paper is to present a newly developed pressure-based solution procedure that is equally valid at all Reynolds and Mach number values. The collocated variable algorithm is formulated on a non-orthogonal coordinate system using Cartesian velocity components. The method is easy to implement, highly accurate, and does not require any explicit addition of damping terms to stabilize it or to properly resolve shock waves. Moreover, the algorithm will have two new features. The first one is the use of the Normalized Variable Formulation (NVF) [24] and/or the Normalized Variable and Space Formulation (NVSF) [25] methodology in the discretization of the convective terms. To the authors' knowledge, the NVF/NVSF methodologies have never been used to bound the convective flux in compressible flows. Mainly low order schemes or the TVD [26] formulation has usually been adopted. The second one is the use of High-Resolution (HR) schemes in the interpolation of density appearing in the mass fluxes in order to enhance the shock capturing capability of the method.

In what follows the governing equations for compressible flows are presented and their discretization detailed so as to lay the ground for the derivation of the pressure-correction equation. Then, a brief description of the various types of boundary conditions for both incompressible and compressible flows is given. Finally, the increase in accuracy with the use of HR schemes for density is demonstrated. This is done by comparing predictions, for a number of

problems, obtained using the third-order SMART scheme [8] for all variables except density (for which the Upwind [1] scheme is used) against another set of results obtained using the SMART scheme for all variables including density. Results generated using a number of other HR schemes are also presented.

GOVERNING EQUATIONS

The equations governing the flow of a two-dimensional compressible fluid are the continuity equation, the momentum equations, and the energy equation. This set of non-linear, coupled equations is solved for the unknowns ρ , \mathbf{v} , T and P . In vector form, these equations may be written as:

$$\frac{\partial \rho}{\partial t} + \nabla \cdot (\rho \mathbf{v}) = 0 \quad (1)$$

$$\frac{\partial (\rho \mathbf{v})}{\partial t} + \nabla \cdot (\rho \mathbf{v} \mathbf{v}) = -\nabla P + \nabla \cdot (\mu \nabla \mathbf{v}) + \frac{1}{3} \nabla (\mu \nabla \cdot \mathbf{v}) \quad (2)$$

$$\frac{\partial (\rho T)}{\partial t} + \nabla \cdot (\rho \mathbf{v} T) = \frac{1}{c_p} \left\{ \nabla \cdot (\mathbf{k} \nabla T) + \beta T \left[\frac{\partial P}{\partial t} + \nabla \cdot (P \mathbf{v}) - P \nabla \cdot (\mathbf{v}) \right] + \Phi + \dot{q} \right\} \quad (3)$$

where

$$\Phi = \mu \left\{ 2 \left[\left(\frac{\partial u}{\partial x} \right)^2 + \left(\frac{\partial v}{\partial y} \right)^2 \right] + \left(\frac{\partial u}{\partial y} + \frac{\partial v}{\partial x} \right)^2 - \frac{2}{3} (\nabla \cdot \mathbf{v})^2 \right\} \quad (4)$$

and β the thermal expansion coefficient which is equal to $1/T$ for an ideal fluid.

In addition to the above differential equations, an auxiliary equation of state relating density to pressure and temperature ($\rho = f(P, T)$) is needed. For an ideal fluid, this equation is given by:

$$\rho = \frac{P}{RT} = C_p P \quad (5)$$

where R is the gas constant.

A review of the above differential equations reveals that they are similar in structure. If a typical representative variable is denoted by ϕ , the general differential equation may be written as,

$$\frac{\partial(\rho\phi)}{\partial t} + \nabla \cdot (\rho \mathbf{v} \phi) = \nabla \cdot (\Gamma^\phi \nabla \phi) + Q^\phi \quad (6)$$

where the expressions for Γ^ϕ and Q^ϕ can be deduced from the parent equations. The four terms in the above equation describe successively unsteadiness, convection (or advection), diffusion, and generation/dissipation effects. In fact, all terms not explicitly accounted for in the first three terms are included in the catchall source term Q^ϕ .

FINITE VOLUME DISCRETIZATION

The general transport equation (Eq. (6)) is discretized using the control volume methodology. The discretization process is a two-level procedure. In level I, the equations are integrated over a control volume so as to get a discretized description of the conservation laws. In level II, an interpolation profile is used to relate the discretized terms of level I to the discrete nodes in the solution domain.

LEVEL I DISCRETIZATION

The integral form of equation (6), obtained by applying the divergence theorem over the control volume P shown in Fig. 1, may be written as:

$$\int_{\Omega} \frac{\partial(\rho\phi)}{\partial t} d\Omega + \oint_S (\rho\mathbf{v}\phi - \Gamma^{\phi}\nabla\phi) \cdot d\mathbf{S} = \int_{\Omega} Q^{\phi} d\Omega \quad (7)$$

where Ω is the volume of cell P. Replacing the surface integral over the control volume by a discrete summation of the flux terms over the sides of the control volume, equation (7) becomes:

$$\frac{\partial}{\partial t} [(\rho\phi)_P] \Omega + \Delta [(\rho\mathbf{v}\phi - \Gamma^{\phi}\nabla\phi) \cdot \mathbf{S}]_P = Q^{\phi} \Omega \quad (8)$$

In the above equation, the discretized form of the unsteady term will be detailed later, and the Δ operator is the discretized version of the surface integral defined by:

$$\Delta[\phi]_P = \phi_e + \phi_w + \phi_n + \phi_s \quad (9)$$

Hence equation (8) can be written as

$$\frac{\partial}{\partial t} [(\rho\phi)_P] \Omega + \Delta[J]_P = \frac{\partial}{\partial t} [(\rho\phi)_P] \Omega + (J_e + J_w + J_n + J_s) = Q^{\phi} \Omega \quad (10)$$

where J_f represents the total flux of ϕ across face 'f' and is given by

$$J_f = (\rho\mathbf{v}\phi - \Gamma^{\phi}\nabla\phi)_f \cdot \mathbf{S}_f \quad (11)$$

The flux J_f is a combination of the convection flux $J_f^C = (\rho\mathbf{v}\phi)_f \cdot \mathbf{S}_f$ and diffusion flux

$$J_f^D = (-\Gamma^{\phi}\nabla\phi)_f \cdot \mathbf{S}_f.$$

LEVEL II DISCRETIZATION

From equation (10), it is obvious that the total fluxes are needed at the control volume faces where the values of the dependent variables are not available and should be obtained by interpolation. Therefore, the accuracy of the solution depends on the proper estimation of these values as a function of the neighboring ϕ node values. Through the use of an interpolation profile, or an

estimate of how ϕ varies between nodes, the approximation scheme produces an expression for the face value which is dependent on the nodal ϕ values in the vicinity of the face. Details regarding the profile assumption are presented next.

Discretization of the Unsteady Term

For the representation of the unsteady term, the grid-point value of ϕ is assumed to prevail throughout the control volume. Then, as used earlier,

$$\int_{\Omega} \frac{\partial(\rho\phi)}{\partial t} d\Omega = \frac{\partial}{\partial t} [(\rho\phi)_P] \Omega \quad (12)$$

The time derivative is approximated using the following Euler-implicit formulation:

$$\frac{\partial}{\partial t} [(\rho\phi)_P] = \frac{(\rho_P \phi_P - \rho_P^o \phi_P^o)}{\delta t} \quad (13)$$

In the above equation, δt represents the time step and the superscript o denotes values at time $(t-\delta t)$.

Discretization of the Diffusion Flux J_f^D

The diffusion flux J_f^D is discretized along each surface of the control volume using the method described in Zwart et al. [27] according to which it is decomposed into:

$$(-\Gamma^\phi \nabla \phi)_f \cdot \mathbf{S}_f = (-\Gamma^\phi \nabla \phi)_f \cdot \hat{\mathbf{n}}_f S_f = -\Gamma_f^\phi [(\nabla \phi)_f \cdot (\gamma \hat{\mathbf{d}})_f + (\overline{\nabla \phi})_f \cdot (\hat{\mathbf{n}}_f - (\gamma \hat{\mathbf{d}})_f)] S_f \quad (14)$$

where $(\overline{\nabla \phi})_f$ is the average of the adjacent cell gradients, $\hat{\mathbf{n}}_f$ and $\hat{\mathbf{d}}_f$ (Fig. 2) are the contravariant (surface vector) and covariant (curvilinear coordinate) unit vectors respectively, and γ is a scaling factor. This factor is chosen such that it

is equal to 1 on orthogonal meshes in order for the method to collapse to classical stencils [27,28]. With that constraint, the expression for γ on structured meshes is:

$$\gamma_f = \frac{1}{\hat{\mathbf{n}}_f \cdot \hat{\mathbf{d}}_f} = \frac{\mathbf{S}_f \cdot \mathbf{d}_f}{\mathbf{S}_f \cdot \mathbf{d}_f} \quad (15)$$

Defining the space vector $\hat{\mathbf{e}}_f$ as:

$$\hat{\mathbf{e}}_f = (\hat{\mathbf{n}}_f - (\gamma \hat{\mathbf{d}})_f) \mathbf{S}_f = \kappa_f^x \mathbf{i} + \kappa_f^y \mathbf{j} \quad (16)$$

the expression for $(-\Gamma^\phi \nabla \phi)_f \cdot \mathbf{S}_f$ becomes,

$$(-\Gamma^\phi \nabla \phi)_f \cdot \mathbf{S}_f = -\Gamma_f^\phi \left[(\nabla \phi)_f \cdot (\hat{\mathbf{d}})_f \frac{\mathbf{S}_f \cdot \mathbf{d}_f}{\mathbf{S}_f \cdot \mathbf{d}_f} \mathbf{S}_f + (\overline{\nabla \phi})_f \cdot (\kappa_f^x \mathbf{i} + \kappa_f^y \mathbf{j}) \right] \quad (17)$$

In this form, the term $(\nabla \phi)_f \cdot (\hat{\mathbf{d}})_f$ represents the gradient in the direction of the coordinate line joining P and F (see Figure 2). Therefore, the above equation can be rewritten as:

$$(-\Gamma^\phi \nabla \phi)_f \cdot \mathbf{S}_f = -\Gamma_f^\phi \left[\frac{\phi_F - \phi_P}{d_f} \frac{\mathbf{S}_f \cdot \mathbf{d}_f}{\mathbf{S}_f \cdot \mathbf{d}_f} \mathbf{S}_f + (\overline{\nabla \phi})_f \cdot (\kappa_f^x \mathbf{i} + \kappa_f^y \mathbf{j}) \right] \quad (18)$$

and upon simplifying, it reduces to:

$$(-\Gamma^\phi \nabla \phi)_f \cdot \mathbf{S}_f = -\Gamma_f^\phi \left[(\phi_F - \phi_P) \frac{\mathbf{S}_f \cdot \mathbf{S}_f}{\mathbf{S}_f \cdot \mathbf{d}_f} + (\overline{\nabla \phi})_f \cdot (\kappa_f^x \mathbf{i} + \kappa_f^y \mathbf{j}) \right] \quad (19)$$

The $(\overline{\nabla \phi})_f$ is calculated as:

$$(\overline{\nabla \phi})_f = f_f (\nabla \phi)_P + (1 - f_f) (\nabla \phi)_F \quad (20)$$

and the gradient at the main grid point F (F= P, E, W, N, or S) is obtained from:

$$\begin{aligned}
(\nabla\phi)_F &= \frac{1}{\Omega} \int_{\Omega} \nabla\phi d\Omega = \frac{1}{\Omega} \oint_S \phi d\mathbf{S} = \frac{1}{\Omega} (\phi_{Fe} \mathbf{S}_{Fe} + \phi_{Fw} \mathbf{S}_{Fw} + \phi_{Fn} \mathbf{S}_{Fn} + \phi_{Fs} \mathbf{S}_{Fs}) \\
&= \frac{1}{\Omega} (\phi_{Fe} S_{Fe}^x + \phi_{Fw} S_{Fw}^x + \phi_{Fn} S_{Fn}^x + \phi_{Fs} S_{Fs}^x) \mathbf{i} + \\
&\quad \frac{1}{\Omega} (\phi_{Fe} S_{Fe}^y + \phi_{Fw} S_{Fw}^y + \phi_{Fn} S_{Fn}^y + \phi_{Fs} S_{Fs}^y) \mathbf{j} \\
&= (\nabla\phi)_F^x \mathbf{i} + (\nabla\phi)_F^y \mathbf{j}
\end{aligned} \tag{21}$$

The final form of the diffusive flux along face f ($f=e, w, n, \text{ or } s$) is:

$$\begin{aligned}
(-\Gamma^\phi \nabla\phi)_f \cdot \mathbf{S}_f &= -\Gamma_f^\phi (\phi_F - \phi_P) \frac{(S_f^x)^2 + (S_f^y)^2}{S_f^x d_f^x + S_f^y d_f^y} - \\
&\quad \underbrace{\Gamma_f^\phi \left\{ [f_f (\nabla\phi)_P^x + (1-f_f)(\nabla\phi)_F^x] \kappa_f^x + [f_f (\nabla\phi)_P^y + (1-f_f)(\nabla\phi)_F^y] \kappa_f^y \right\}}_{\text{cross-diffusion contribution}}
\end{aligned} \tag{22}$$

The underlined part of the diffusion flux is called the cross-diffusion contribution.

It vanishes when the grid is orthogonal, and is small compared to normal diffusion for nearly orthogonal grid. In such circumstances, explicit treatment of the cross diffusion term does not significantly influence the rate of convergence of the overall solution procedure and simplifies the matrix of coefficients.

Discretization of the Convection Flux J_f^C

The convection flux of ϕ through the control volume face f is given by :

$$J_f^C = (\rho v \phi)_f \cdot \mathbf{S}_f = F_f \phi_f \tag{23}$$

where ϕ_f stands for the mean value of ϕ along cell face f , and $F_f = (\rho v \cdot \mathbf{S})_f$ is the mass flow rate across face f . Using some assumed interpolation profile, ϕ_f can be explicitly formulated by a functional relationship of the form:

$$\phi_f = f(\phi_{nb}) \tag{24}$$

where ϕ_{nb} denotes the ϕ values at the neighboring nodes. The interpolation profile to be used should be bounded in order not to give rise to the well-known dispersion error problem [2]. In this work, HR schemes formulated in the

context of the NVSF methodology, which is explained in the next section, are used. Since these interpolation profiles may involve a large number of neighboring points, the solution of the resultant system of equations can become very expensive computationally, hence the use of a compacting procedure is most welcome. For that purpose, the deferred correction method [29,30] is adopted. With this approach, the convection is split into an implicit part, expressed through first order upwind differencing scheme (UDS) [1], and an explicit part, which equals the difference between the UDS and HR approximations, i.e.:

$$F_f \phi_f = F_f \phi_f^U + F_f (\phi_f^{HR} - \phi_f^U) \quad (25)$$

The deferred correction approach enhances the diagonal dominance of the matrix of coefficient, which adds to the stability of the solution algorithm.

Discretization of the Sources

The integral value of the source term over the control volume P (Fig. 1) is obtained by assuming the estimate of the source at the control volume center to represent the mean value over the whole control volume. Hence, one can write:

$$\int_{\Omega} Q^{\phi} d\Omega = Q^{\phi} \Omega \quad (26)$$

Following the practice adopted in Patankar [1], the source term is linearized according to:

$$Q^{\phi} = Q_C^{\phi} + Q_P^{\phi} \phi \quad (27)$$

where Q_P^{ϕ} should always be a negative quantity. Moreover, the additional terms, appearing in the momentum and energy equations, not featured in

equation (11), are treated explicitly and their discretization is analogous to that of the ordinary diffusion flux.

ALGEBRAIC SYSTEM OF EQUATIONS

The discretized equation, Eq. (10), is transformed into an algebraic equation at the main grid point P by substituting the fluxes at all faces of the control volume by their equivalent expressions. Then, performing some algebraic manipulations on the resultant equation, the following algebraic relation, linking the value of the dependent variable at the control volume center to the neighboring values, is obtained:

$$a_P^\phi \phi_P = \sum_{NB(P)} a_{NB}^\phi \phi_{NB} + b_P^\phi \quad (28)$$

In the above equation, a_{NB}^ϕ are the coefficients multiplying the value of ϕ at the neighboring nodes $NB=(E, W, N, \text{ and } S)$ surrounding the central node P, a_P^ϕ is the coefficient of ϕ_P , and b_P^ϕ contains all terms that are not expressed through the nodal values of the dependent variable (e.g. the source term Q^ϕ , the pressure gradients in the momentum equations, terms involving known values of ϕ etc. ...). The final form of these coefficients is as follows:

$$a_E^\phi = \Gamma_e^\phi \frac{(S_e^x)^2 + (S_e^y)^2}{S_e^x d_e^x + S_e^y d_e^y} + \parallel -F_e, 0 \parallel \quad (29)$$

$$a_W^\phi = \Gamma_w^\phi \frac{(S_w^x)^2 + (S_w^y)^2}{S_w^x d_w^x + S_w^y d_w^y} + \parallel -F_w, 0 \parallel \quad (30)$$

$$a_N^\phi = \Gamma_n^\phi \frac{(S_n^x)^2 + (S_n^y)^2}{S_n^x d_n^x + S_n^y d_n^y} + \parallel -F_n, 0 \parallel \quad (31)$$

$$a_S^\phi = \Gamma_s^\phi \frac{(S_s^x)^2 + (S_s^y)^2}{S_s^x d_s^x + S_s^y d_s^y} + \parallel -F_s, 0 \parallel \quad (32)$$

$$a_p^\phi = a_E^\phi + a_W^\phi + a_N^\phi + a_S^\phi + a_P^\phi - Q_P^\phi \Omega \quad (33)$$

$$a_p^\phi = \frac{\rho_P^\phi \Omega}{\Delta t} \quad (34)$$

$$\begin{aligned} b_p^\phi = & Q_C^\phi \Omega + a_P^\phi \phi_P^\phi - \left[F_e (\phi_e^{\text{HR}} - \phi_e^U) + F_w (\phi_w^{\text{HR}} - \phi_w^U) + F_n (\phi_n^{\text{HR}} - \phi_n^U) + F_s (\phi_s^{\text{HR}} - \phi_s^U) \right] \\ & + \Gamma_e^\phi \left\{ \left[f_e (\nabla \phi)_P^x + (1 - f_e) (\nabla \phi)_E^x \right] \kappa_e^x + \left[f_e (\nabla \phi)_P^y + (1 - f_e) (\nabla \phi)_E^y \right] \kappa_e^y \right\} \\ & + \Gamma_w^\phi \left\{ \left[f_w (\nabla \phi)_P^x + (1 - f_w) (\nabla \phi)_W^x \right] \kappa_w^x + \left[f_w (\nabla \phi)_P^y + (1 - f_w) (\nabla \phi)_W^y \right] \kappa_w^y \right\} \\ & + \Gamma_n^\phi \left\{ \left[f_n (\nabla \phi)_P^x + (1 - f_n) (\nabla \phi)_N^x \right] \kappa_n^x + \left[f_n (\nabla \phi)_P^y + (1 - f_n) (\nabla \phi)_N^y \right] \kappa_n^y \right\} \\ & + \Gamma_s^\phi \left\{ \left[f_s (\nabla \phi)_P^x + (1 - f_s) (\nabla \phi)_S^x \right] \kappa_s^x + \left[f_s (\nabla \phi)_P^y + (1 - f_s) (\nabla \phi)_S^y \right] \kappa_s^y \right\} \end{aligned} \quad (35)$$

For the solution domain as a whole there results a system of N equations in N unknowns, where N is the number of control volumes. Many techniques exist for solving large systems of linear equations that may be classified as direct or iterative methods. The use of direct methods is not appropriate in the present context because they require much more storage than iterative methods and are usually more expensive computationally. Owing to the non-linear nature of the set of equations, the discretized equations are solved by the use of iterative methods. Current iterative methods differ with respect to storage requirement and degree of implicitness, such as the point-by-point successive over-relaxation method [31], the strongly implicit procedure of Stone [32] and its variations, the Incomplete Cholesky Conjugent Gradient (ICCG) [33], or the Multigrid Method of Brandt [34] to site a few. Although these methods have their own desirable attributes, the degree of simplicity of their implementation in a computer code is approximately inversely proportional to their rate of convergence. The algorithm used in this work is the TDMA [35].

During the iterative process, it is often desirable to slow the changes, from iteration to iteration, in the values of the dependent variable. This process is called under-relaxation. It is an important tool that prevents divergence of the

iterative solution for strongly nonlinear problems, as is the case here. If ϕ_p^* and ϕ_p are the values from the previous and current iterations, respectively, then Eq. (28) can be written as

$$\phi_p = \phi_p^* + \left(\frac{\sum_{NB(P)} a_{NB}^\phi \phi_{NB} + b_p^\phi}{a_p^\phi} - \phi_p^* \right) \quad (36)$$

In the above equation, the underlined term represents the change in ϕ_p produced by the current iteration. This change can be varied by introducing an under-relaxation factor α ($0 \leq \alpha \leq 1$), so that

$$\phi_p = \phi_p^* + \alpha \left(\frac{\sum_{NB(P)} a_{NB}^\phi \phi_{NB} + b_p^\phi}{a_p^\phi} - \phi_p^* \right) \quad (37)$$

or

$$\frac{a_p^\phi}{\alpha} \phi_p = \sum_{NB(P)} a_{NB}^\phi \phi_{NB} + b_p^\phi + (1 - \alpha) \frac{a_p^\phi}{\alpha} \phi_p^* \quad (38)$$

At the state of convergence, ϕ_p^* and ϕ_p are equal and the original equation is satisfied. There is no general rule for choosing the optimum value of α and a suitable one for a given problem is usually found from exploratory computations. Equation (38) can be rewritten in the form of equation (28) by redefining a_p^ϕ and b_p^ϕ as follows:

$$\begin{cases} a_p^\phi \leftarrow \frac{a_p^\phi}{\alpha} \\ b_p^\phi \leftarrow b_p^\phi + (1 - \alpha) \frac{a_p^\phi}{\alpha} \phi_p^* \end{cases} \quad (39)$$

THE NVSF METHODOLOGY FOR CONSTRUCTING HR SCHEMES

As mentioned earlier, the discretization of the convection flux is not straightforward and requires additional attention. Since the intention is to develop a high-resolution algorithm, the highly diffusive first order UPWIND scheme [1] is excluded. As such, a high order interpolation profile is sought. The difficulties associated with the use of such profiles stem from the conflicting requirements of accuracy, stability, and boundedness. Solutions predicted with high order profiles tend to provoke oscillations in the solution when the local Peclet number is high in combination with steep gradients of the flow properties. To suppress these oscillations, many techniques have been advertised and may be broadly classified into two groups: the flux blending method [36,37,38,39] and the composite flux limiter method [8,24-26,40], the latter being the one adopted here. In this technique, the numerical flux at the interface of the computational cell is modified by employing a flux limiter that enforces boundedness. The formulation of high-resolution flux limiter schemes on uniform grid has recently been generalized by Leonard [24,40] through the Normalized Variable Formulation (NVF) methodology and on non-uniform grid by Darwish and Moukalled [25] through the Normalized Variable and Space Formulation (NVSF) methodology. The NVF and NVSF methodologies have provided a good framework for the development of HR schemes that combine simplicity of implementation with high accuracy and boundedness. Moreover, to the authors' knowledge, the NVSF formulation has never been used to bound the convection flux in compressible flows. It is an objective of this work to

extend the applicability of this technique to compressible flows. Therefore, before introducing the high-resolution algorithm, a brief review of the NVSF methodology is in order. This is done by first defining the Normalized Variables, then presenting the Convection Boundedness Criterion (CBC) [8], and finally describing the various HR schemes employed in this work (OSHER [41], MUSCL [42], CLAM [43], SMART [8], EXPONENTIAL [24], SUPER-C [44], and ISNAS [45]).

NORMALIZED VARIABLES

Fig. 3(a) shows the local behavior of the convected variable near a control-volume face. The node labeling refers to the upstream, central, and downstream grid points designated by U, C, and D, located at distances ξ_U , ξ_C and ξ_D from the origin, respectively. The values of ϕ at these nodes are designated by ϕ_U , ϕ_C and ϕ_D respectively. Moreover, the value of the dependent variable at the control volume face located at a distance ξ_f from the origin is expressed by ϕ_f . With this notation, the normalized variables are defined as follows:

$$\tilde{\phi} = \frac{\phi - \phi_U}{\phi_D - \phi_U} \quad \tilde{\xi} = \frac{\xi - \xi_U}{\xi_D - \xi_U} \quad (40)$$

The use of the above-normalized parameters simplifies the functional representation of interpolation schemes (Fig. 3(b)) and helps defining the stability and boundedness conditions that they should satisfy. In addition, the normalized functional relationship of any scheme may be plotted on a Normalized Variable Diagram (NVD) (Fig. 3(c)), which is an effective tool in

assessing the accuracy, boundedness, and relative diffusivity of convective schemes. In general, the value of ϕ_f is represented by the following parametric relation:

$$\phi_f = f(\phi_U, \phi_C, \phi_D, \xi_U, \xi_C, \xi_f, \xi_D) \quad (41)$$

which, upon normalizing, is simplified to

$$\tilde{\phi}_f = f(\tilde{\phi}_C, \tilde{\xi}_C, \tilde{\xi}_f) \quad (42)$$

By comparing equations (41) and (42) it is clear that one of the normalization benefits is to reduce the number of parameters involved in the functional relationship.

THE CONVECTIVE BOUNDEDNESS CRITERION (CBC)

Based on the normalized variable analysis, Gaskell and Lau [8] formulated a convection boundedness criterion (CBC) for implicit steady flow calculation. This CBC states that for a scheme to have the boundedness property its functional relationship should be continuous, should be bounded from below by $\tilde{\phi}_f = \tilde{\phi}_C$, from above by unity, and should pass through the points (0,0) and (1,1), in the monotonic range ($0 < \tilde{\phi}_C < 1$), and for $1 < \tilde{\phi}_C$ or $\tilde{\phi}_C < 0$, the functional relationship $f(\tilde{\phi}_C)$ should equal $\tilde{\phi}_C$. Mathematically, these conditions are

$$\text{CBC} = \begin{cases} f(\tilde{\phi}) & \text{is continuous} \\ f(\tilde{\phi}) = 0 & \text{for } \tilde{\phi}_C = 0 \\ f(\tilde{\phi}) = 1 & \text{for } \tilde{\phi}_C = 1 \\ 1 < f(\tilde{\phi}) < \tilde{\phi}_C & \text{for } 0 < \tilde{\phi}_C < 1 \\ f(\tilde{\phi}) = \tilde{\phi}_C & \text{for } \tilde{\phi}_C < 0 \text{ and } \tilde{\phi}_C > 1 \end{cases} \quad (43)$$

The above conditions may also be illustrated on a Normalized Variable Diagram (NVD) as shown in Fig. 3(c).

NORMALIZED VARIABLE AND SPACE FORMULATION (NVSF) METHODOLOGY

Knowing the required conditions for boundedness, the shortcomings of the High Order (HO) schemes were eliminated through the development of HR schemes satisfying all above requirements. Without going into details, a number of HR schemes were formulated using the NVF/NVSF methodologies and the functional relationships for the ones used in this work are given below. For more details the reader is referred to Darwish and Moukalled [25].

OSHER

$$\tilde{\phi}_f = \begin{cases} \frac{\tilde{\xi}_f}{\tilde{\xi}_C} \tilde{\phi}_C & 0 < \tilde{\phi}_C < \frac{\tilde{\xi}_C}{\tilde{\xi}_f} \\ 1 & \frac{\tilde{\xi}_C}{\tilde{\xi}_f} \leq \tilde{\phi}_C < 1 \\ \tilde{\phi}_C & \text{elsewhere} \end{cases} \quad (44)$$

MUSCL

$$\tilde{\phi}_f = \begin{cases} \frac{2\tilde{\xi}_f - \tilde{\xi}_C}{\tilde{\xi}_C} \tilde{\phi}_C & 0 < \tilde{\phi}_C < \frac{\tilde{\xi}_C}{2} \\ \tilde{\phi}_C + (\tilde{\xi}_f - \tilde{\xi}_C) & \frac{\tilde{\xi}_C}{2} \leq \tilde{\phi}_C < 1 + \tilde{\xi}_C - \tilde{\xi}_f \\ 1 & 1 + \tilde{\xi}_C - \tilde{\xi}_f \leq \tilde{\phi}_C < 1 \\ \tilde{\phi}_C & \text{elsewhere} \end{cases} \quad (45)$$

CLAM

$$\tilde{\phi}_f = \begin{cases} \frac{(\tilde{\xi}_C^2 - \tilde{\xi}_f)}{\tilde{\xi}_C(\tilde{\xi}_C - 1)} \tilde{\xi}_C + \frac{(\tilde{\xi}_f - \tilde{\xi}_C)}{\tilde{\xi}_C(\tilde{\xi}_C - 1)} \tilde{\xi}_C^2 & 0 < \tilde{\phi}_C < 1 \\ \tilde{\phi}_C & \text{elsewhere} \end{cases} \quad (46)$$

EXPONENTIAL

$$\tilde{\phi}_f = \begin{cases} 1.125(1 - e^{-2.19722\tilde{\phi}_C}) & 0 < \tilde{\phi}_C < 1 \\ \tilde{\phi}_C & \text{elsewhere} \end{cases} \quad (47)$$

SMART

$$\tilde{\phi}_f = \begin{cases} \frac{\tilde{\xi}_f(1 - 3\tilde{\xi}_C + 2\tilde{\xi}_f)}{\tilde{\xi}_C(1 - \tilde{\xi}_C)} \tilde{\phi}_C & 0 < \tilde{\phi}_C < \frac{\tilde{\xi}_C}{3} \\ \frac{\tilde{\xi}_f(1 - \tilde{\xi}_f)}{\tilde{\xi}_C(1 - \tilde{\xi}_C)} \tilde{\phi}_C + \frac{\tilde{\xi}_f(\tilde{\xi}_f - \tilde{\xi}_C)}{1 - \tilde{\xi}_C} & \frac{\tilde{\xi}_C}{3} \leq \tilde{\phi}_C < \frac{\tilde{\xi}_C}{\tilde{\xi}_f}(1 + \tilde{\xi}_f - \tilde{\xi}_C) \\ 1 & \frac{\tilde{\xi}_C}{\tilde{\xi}_f}(1 + \tilde{\xi}_f - \tilde{\xi}_C) \leq \tilde{\phi}_C < 1 \\ \tilde{\phi}_C & \text{elsewhere} \end{cases} \quad (48)$$

SUPER-C

$$\tilde{\phi}_f = \begin{cases} \frac{\tilde{\xi}_f(1 - 3\tilde{\xi}_C + 2\tilde{\xi}_f)}{\tilde{\xi}_C(1 - \tilde{\xi}_C)} \tilde{\phi}_C & 0 < \tilde{\phi}_C < \frac{2}{5}\tilde{\xi}_C \\ \frac{1 - \tilde{\xi}_f}{1 - \tilde{\xi}_C} \tilde{\phi}_C + \frac{\tilde{\xi}_f - \tilde{\xi}_C}{1 - \tilde{\xi}_C} & \frac{2}{5}\tilde{\xi}_C \leq \tilde{\phi}_C < \tilde{\xi}_C \\ \frac{\tilde{\xi}_f(1 - \tilde{\xi}_f)}{\tilde{\xi}_C(1 - \tilde{\xi}_C)} \tilde{\phi}_C + \frac{\tilde{\xi}_f(\tilde{\xi}_f - \tilde{\xi}_C)}{1 - \tilde{\xi}_C} & \tilde{\xi}_C \leq \tilde{\phi}_C < \frac{\tilde{\xi}_C}{\tilde{\xi}_f}(1 + \tilde{\xi}_f - \tilde{\xi}_C) \\ 1 & \frac{\tilde{\xi}_C}{\tilde{\xi}_f}(1 + \tilde{\xi}_f - \tilde{\xi}_C) < \tilde{\phi}_C < 1 \\ \tilde{\phi}_C & \text{elsewhere} \end{cases} \quad (49)$$

ISNAS

$$\tilde{\phi}_f = \begin{cases} \frac{(\tilde{\xi}_f - \tilde{\xi}_c)^2}{\tilde{\xi}_c^2(1 - \tilde{\xi}_c)^2} \tilde{\phi}_c^3 - \frac{(2\tilde{\xi}_c^3 + \tilde{\xi}_c\tilde{\xi}_f^2 - \tilde{\xi}_c\tilde{\xi}_f + \tilde{\xi}_f^2 - 3\tilde{\xi}_c^2\tilde{\xi}_f)}{\tilde{\xi}_c^2(1 - \tilde{\xi}_c)^2} \tilde{\phi}_c^2 \\ \quad + \frac{(\tilde{\xi}_c^3 - 3\tilde{\xi}_c\tilde{\xi}_f + \tilde{\xi}_f^2 + \tilde{\xi}_f)}{\tilde{\xi}_c(1 - \tilde{\xi}_c)^2} \tilde{\phi}_c & 0 < \tilde{\phi}_c < 1 \\ \tilde{\phi}_c & \text{elsewhere} \end{cases} \quad (50)$$

HIGH RESOLUTION ALGORITHM

The need for a solution algorithm arises in the simulation of flow problems because a scalar equation does not exist for pressure. Rather, the pressure field acts indirectly on the velocity field to constrain it to satisfy the continuity equation. Hence, if a segregated approach is to be adopted, coupling between the u , v , p , and P primitive variables in the continuity and momentum equations will be required. Evidently, the whole set of equations could be solved directly (after linearization) since the number of equations equals the number of unknowns. However, the computational effort and storage requirements needed by such an approach are often prohibitive. This has forced researchers to seek less expensive methods and resulted in the development of several segregated solution algorithms [1,46,47,48,49,50,51,52]. Recently, Moukalled and Darwish presented a unified formulation of these algorithms [53].

The segregated algorithm adopted in this work is the SIMPLE algorithm [1,46], that involves a **predictor** and a **corrector** step. In the **predictor** step, the velocity field is calculated based on a guessed or estimated pressure field. In the **corrector** step, a pressure (or a pressure-correction) equation is derived

and solved. Then, the variation in the pressure field is accounted for within the momentum equations by corrections to the velocity and density fields. Thus, the velocity, density, and pressure fields are driven, iteratively, to better satisfying the momentum and continuity equations simultaneously and convergence is achieved by repeatedly applying the above-described procedure.

Before deriving the pressure or pressure correction equation, the discretized momentum equations are first written in the following notationally more suitable form:

$$\begin{aligned} a_P^u u_P &= \sum_{NB(P)} a_{NB}^u u_{NB} + b_P^u - \Omega (\nabla P)_P \cdot \mathbf{i} \\ a_P^v v_P &= \sum_{NB(P)} a_{NB}^v v_{NB} + b_P^v - \Omega (\nabla P)_P \cdot \mathbf{j} \end{aligned} \quad (51)$$

This form can be simplified to

$$\begin{Bmatrix} u_P \\ v_P \end{Bmatrix} - \begin{Bmatrix} H[u]_P \\ H[v]_P \end{Bmatrix} = - \begin{Bmatrix} D[u]_P & 0 \\ 0 & D[v]_P \end{Bmatrix} \begin{Bmatrix} (\nabla P)_P \cdot \mathbf{i} \\ (\nabla P)_P \cdot \mathbf{j} \end{Bmatrix} \quad (52)$$

where

$$(\nabla P)_P = \frac{1}{\Omega} \int \nabla P d\Omega \quad H[\phi]_P = \frac{\sum_{NB(P)} a_{NB}^\phi \phi_{NB} + b_P^\phi}{a_P^\phi} \quad D[\phi]_P = \frac{\Omega}{a_P^\phi} \quad (53)$$

In the above equations, Ω is the volume of cell P , and the subscripts e , w , n , and s refer to values at the east, west, north, and south faces of the control volume (Fig. 1). Defining the vector forms of the above operators as,

$$\mathbf{H}[\mathbf{v}]_P = \begin{Bmatrix} H[u]_P \\ H[v]_P \end{Bmatrix} \quad \mathbf{D}_P = \begin{Bmatrix} D[u]_P & 0 \\ 0 & D[v]_P \end{Bmatrix} \quad (\nabla P)_P = \begin{Bmatrix} (\nabla P)_P \cdot \mathbf{i} \\ (\nabla P)_P \cdot \mathbf{j} \end{Bmatrix} = \begin{Bmatrix} (\nabla P)_P^x \\ (\nabla P)_P^y \end{Bmatrix} \quad (54)$$

the momentum equations in vector form become

$$\mathbf{v}_P - \mathbf{H}[\mathbf{v}]_P = -\mathbf{D}_P(\nabla P)_P \quad (55)$$

Since an equation for pressure will be derived by combining momentum and continuity, the discretized form of the continuity equation is needed and is obtained as (Fig.1):

$$\begin{aligned} \int_{\Omega} \frac{\partial \rho}{\partial t} d\Omega + \int_{\Omega} \nabla \cdot (\rho \mathbf{v}) d\Omega &= 0 \\ \frac{(\rho_P - \rho_P^o)}{\delta t} \Omega + \oint_S (\rho \mathbf{v}) \cdot d\mathbf{S} &= 0 \end{aligned} \quad (56)$$

which can be written as

$$\begin{aligned} \frac{(\rho_P - \rho_P^o)}{\delta t} \Omega + \Delta[\rho \mathbf{v} \cdot \mathbf{S}]_P &= 0 \\ \frac{(\rho_P - \rho_P^o)}{\delta t} \Omega + \Delta[\rho U]_P &= 0 \end{aligned} \quad (57)$$

where

$$U_f = \mathbf{v}_f \cdot \mathbf{S}_f \quad (58)$$

For the calculation of the mass fluxes across the control volume faces (U_f) and for checking mass conservation, the values of the velocity components are needed there. In order to avoid oscillations which may result if a simple linear interpolation method is used, a special interpolation practice is employed as suggested by Rhie [54], Peric [38], and Majumbar [55]. The basis for the interpolation procedure are the discretized momentum equations at the control volume centres, as given by equation (55) where the pressure source term has been taken out of the Q^ϕ term and shown explicitly. To evaluate velocities at the control volume face f , terms in equation (55) are selectively interpolated and evaluated at the f location, according to:

$$\mathbf{v}_f - \overline{\mathbf{H}}[\mathbf{v}]_f = -\overline{\mathbf{D}}_f(\nabla P)_f \quad (59)$$

where the overbar denotes a linear interpolation. This relation may be viewed as a pseudo-momentum equation at the control volume face. The cell face velocities are thus made dependent on the pressure difference across the face. This interpolation practice helps avoiding the checkerboard problems previously encountered in collocated variable algorithms [1]. For further details, the reader is referred to Moukalled and Darwish [53].

THE PRESSURE CORRECTION EQUATION

As mentioned earlier, the convergence in the segregated approach is driven by the corrector stage where a pressure (or a pressure-correction) equation is solved. Therefore, the first phase in developing a segregated solution algorithm is to derive such an equation. The key step in the derivation is to note that in the predictor stage a guessed or estimated pressure field from the previous iteration, denoted by $P^{(n)}$, is substituted into the momentum equations. The resulting velocity field, denoted by \mathbf{v}^* , which now satisfies the momentum equations, will not in general satisfy the continuity equation. Thus, a correction is needed in order to obtain velocity and pressure fields that satisfy both equations. Denoting the pressure, velocity, and density corrections by P' , \mathbf{v}' (u' , v'), and ρ' , respectively, the corrected fields are obtained from:

$$\begin{cases} P = P^{(n)} + P' \\ \mathbf{v} = \mathbf{v}^* + \mathbf{v}' & (u = u^* + u', v = v^* + v') \\ \rho = \rho^{(n)} + \rho' \end{cases} \quad (60)$$

Before the pressure field is known, the velocities obtained from the solution of the momentum equations are actually u^* and v^* rather than u and v . Hence the equations solved in the predictor stage are:

$$\mathbf{v}_P^* - \mathbf{H}[\mathbf{v}^*]_P = -\mathbf{D}_P (\nabla P^{(n)})_P \quad (61)$$

while the final solution satisfies

$$\mathbf{v}_P - \mathbf{H}[\mathbf{v}]_P = -\mathbf{D}_P (\nabla P)_P \quad (62)$$

Subtracting the two sets of equation (62) and (61) from each other yields the following equation involving the correction terms:

$$\mathbf{v}'_P - \mathbf{H}[\mathbf{v}']_P = -\mathbf{D}_P (\nabla P')_P \quad (63)$$

Moreover, the new density and velocity fields, ρ and \mathbf{v} , will satisfy the continuity equation if:

$$\frac{(\rho_P - \rho_P^o)}{\delta t} \Omega + \Delta[\rho \mathbf{v} \cdot \mathbf{S}]_P = 0 \quad (64)$$

Linearizing the $(\rho \mathbf{v})$ term, one gets

$$(\rho^* + \rho')(\mathbf{v}^* + \mathbf{v}') = \rho^* \mathbf{v}^* + \rho^* \mathbf{v}' + \rho' \mathbf{v}^* + \rho' \mathbf{v}' \quad (65)$$

Substitution of equation (65) into equation (64) gives

$$\frac{(\rho_P - \rho_P^o)}{\delta t} \Omega + \Delta[(\rho^* \mathbf{v}^* + \rho^* \mathbf{v}' + \rho' \mathbf{v}^* + \rho' \mathbf{v}') \cdot \mathbf{S}]_P = 0 \quad (67)$$

Rearranging, the following equation is obtained:

$$\frac{\Omega}{\delta t} (\rho_P^* + \rho_P') + \Delta[(\rho' \mathbf{v}^* + \rho^* \mathbf{v}') \cdot \mathbf{S}]_P = \frac{\Omega}{\delta t} \rho_P^o - \Delta[(\rho^* \mathbf{v}^*) \cdot \mathbf{S}]_P - \Delta[(\rho' \mathbf{v}') \cdot \mathbf{S}]_P \quad (68)$$

Using equation (63), the above equation becomes:

$$\frac{\Omega}{\delta t} \rho_P' + \Delta[U^* \rho' + \rho^* (\mathbf{H}[\mathbf{v}'] - \mathbf{D}(\nabla P')) \cdot \mathbf{S}]_P = -\frac{(\rho_P^* - \rho_P^o)}{\delta t} \Omega - \Delta[(\rho^* \mathbf{v}^*) \cdot \mathbf{S}]_P - \Delta[(\rho' \mathbf{v}') \cdot \mathbf{S}]_P \quad (69)$$

Finally, substituting density correction by pressure correction, as obtained from the equation of state, the new form of the pressure-correction equation becomes:

$$\frac{\Omega C_n}{\delta t} P'_p + \Delta [C_n U^* P']_p - \Delta [\rho^* \mathbf{D}(\nabla P') \cdot \mathbf{S}]_p = - \frac{(\rho_p^* - \rho_p^o)}{\delta t} \Omega - \Delta [\rho^* U^*]_p - \Delta [\rho^* \mathbf{H}[\mathbf{v}'] \cdot \mathbf{S}]_p - \Delta [(\rho' \mathbf{v}') \cdot \mathbf{S}]_p \quad (70)$$

The usual practice is to neglect the second order correction term $\rho' \mathbf{v}'$. This does not affect neither the convergence rate (i.e. it is considerably smaller than other terms) nor the final solution, since at the state of convergence the correction fields vanish. Furthermore, if the $\mathbf{H}[\mathbf{v}']$ term in the above equation is retained, there will result a pressure correction equation relating the pressure correction value at a point to all values in the domain. Even though such an equation ensures that the corrected fields will satisfy the continuity and momentum equations, it is undesirable because it becomes intractable. To facilitate implementation and reduce cost, this term is neglected in SIMPLE. Therefore, the final form of the pressure-correction equation is:

$$\frac{\Omega C_n}{\delta t} P'_p + \Delta [C_n U^* P']_p - \Delta [\rho^* \mathbf{D}(\nabla P') \cdot \mathbf{S}]_p = - \frac{(\rho_p^* - \rho_p^o)}{\delta t} \Omega - \Delta [\rho^* U^*]_p \quad (71)$$

From the above equation, it is clear that the starred continuity equation appears as a source term in the pressure correction equation. Moreover, in a pressure-based algorithm, the pressure-correction equation is the most important equation that gives the pressure, upon which all other variables are dependent. Therefore, the accuracy of the predictions depends on the proper estimation of pressure from this equation. Definitely, the more accurate the interpolated starred density (ρ^*) values at the control volume faces are, the more accurate the predicted pressure values will be. The use of a central difference scheme for the interpolation of ρ^* leads to instability at Mach numbers near or above 1 [12,15]. On the other hand the use of a first order upwind scheme leads to

excess diffusion [15]. The obvious solution to the aforementioned problems would be to interpolate for values of ρ^* at the control volume faces in the same way interpolation for other dependent variables is carried out: in other words, to employ the bounded HR family of schemes for which no problem-dependent factors are required. Adopting this strategy, the discretized form of the starred steady continuity equation becomes:

$$\Delta[\rho^* U^*]_p = (\rho_e^*)^{HR} U_e^* + (\rho_w^*)^{HR} U_w^* + (\rho_n^*)^{HR} U_n^* + (\rho_s^*)^{HR} U_s^* \quad (72)$$

As can be seen from equation (72), there is no need for any deferred correction and the interpolated starred density values may directly be used. The same procedure is also adopted for calculating the density when computing the mass flow rate at a control volume face in the general conservation equation.

When discretizing the pressure-correction equation (Eq. (71)), careful attention should be paid to the second term on the left hand side that is similar to a convection term and for which any convective scheme may be used. Since at the state of convergence the pressure-correction field is zero, the order of interpolation scheme is not important and does not affect the solution accuracy. Therefore, the use of a first order scheme is sufficient for the purpose of discretizing this term. Adopting the UPWIND scheme [1], the discretized form of the convection-like term $\Delta[C_{\bar{n}} U^* P']_p$ is:

$$\begin{aligned} \Delta[C_{\bar{n}} U^* P']_p &= (C_{\bar{n}} U^* P')_e + (C_{\bar{n}} U^* P')_w + (C_{\bar{n}} U^* P')_n + (C_{\bar{n}} U^* P')_s \\ &= (C_{\bar{n}})_e \left[\|U_e^*, 0\|_{P'_P} - \| -U_e^*, 0\|_{P'_E} \right] + (C_{\bar{n}})_w \left[\|U_w^*, 0\|_{P'_P} - \| -U_w^*, 0\|_{P'_W} \right] + \\ &\quad (C_{\bar{n}})_n \left[\|U_n^*, 0\|_{P'_P} - \| -U_n^*, 0\|_{P'_N} \right] + (C_{\bar{n}})_s \left[\|U_s^*, 0\|_{P'_P} - \| -U_s^*, 0\|_{P'_S} \right] \end{aligned} \quad (73)$$

Rearranging, one obtains:

$$\Delta[C_{\bar{n}} U^* P']_p = [(C_{\bar{n}})_e \|U^*_e, 0\| + (C_{\bar{n}})_w \|U^*_w, 0\| + (C_{\bar{n}})_n \|U^*_n, 0\| + (C_{\bar{n}})_s \|U^*_s, 0\|] P'_p - (C_{\bar{n}})_e \| -U^*_e, 0\| P'_E - (C_{\bar{n}})_w \| -U^*_w, 0\| P'_W - (C_{\bar{n}})_n \| -U^*_n, 0\| P'_N - (C_{\bar{n}})_s \| -U^*_s, 0\| P'_S \quad (74)$$

The term $\Delta[\rho^* \mathbf{D}(\nabla P') \mathbf{S}]_p$ is discretized following the same procedure that was used in discretizing the diffusion flux. Its final form is given by:

$$\begin{aligned} \Delta[\rho^* \mathbf{D}(\nabla P') \mathbf{S}]_p &= (\rho^* \mathbf{D}(\nabla P') \mathbf{S})_e + (\rho^* \mathbf{D}(\nabla P') \mathbf{S})_w + (\rho^* \mathbf{D}(\nabla P') \mathbf{S})_n + (\rho^* \mathbf{D}(\nabla P') \mathbf{S})_s \\ &= \rho^*_e \frac{\bar{D}[u]_e (S^x_e)^2 + \bar{D}[v]_e (S^y_e)^2}{\mathbf{S}_e \cdot \mathbf{d}_e} (P'_E - P'_p) + \rho^*_e \left(\bar{D}[u]_e (\overline{\nabla P'})^x_e \kappa^x_e + \bar{D}[v]_e (\overline{\nabla P'})^y_e \kappa^y_e \right) \\ &\quad + \rho^*_w \frac{\bar{D}[u]_w (S^x_w)^2 + \bar{D}[v]_w (S^y_w)^2}{\mathbf{S}_w \cdot \mathbf{d}_w} (P'_w - P'_p) + \rho^*_w \left(\bar{D}[u]_w (\overline{\nabla P'})^x_w \kappa^x_w + \bar{D}[v]_w (\overline{\nabla P'})^y_w \kappa^y_w \right) \\ &\quad + \rho^*_n \frac{\bar{D}[u]_n (S^x_n)^2 + \bar{D}[v]_n (S^y_n)^2}{\mathbf{S}_n \cdot \mathbf{d}_n} (P'_N - P'_p) + \rho^*_n \left(\bar{D}[u]_n (\overline{\nabla P'})^x_n \kappa^x_n + \bar{D}[v]_n (\overline{\nabla P'})^y_n \kappa^y_n \right) \\ &\quad + \rho^*_s \frac{\bar{D}[u]_s (S^x_s)^2 + \bar{D}[v]_s (S^y_s)^2}{\mathbf{S}_s \cdot \mathbf{d}_s} (P'_S - P'_p) + \rho^*_s \left(\bar{D}[u]_s (\overline{\nabla P'})^x_s \kappa^x_s + \bar{D}[v]_s (\overline{\nabla P'})^y_s \kappa^y_s \right) \end{aligned} \quad (75)$$

where the underlined terms account for the non-orthogonal factors. They are usually neglected since their contribution is small in comparison with other terms and vanish when the grid is orthogonal. However, they could be accounted for by moving them to the right hand side, adding them to the source term, and modifying the solver to explicitly update their values after a solver (not global) iteration. Neglecting these terms, Eq. (75) becomes:

$$\begin{aligned}
\Delta[\rho^* \mathbf{D}(\nabla P') \cdot \mathbf{S}]_P &= \rho_e^* \frac{\overline{D}[u]_e (S_e^x)^2 + \overline{D}[v]_e (S_e^y)^2}{\mathbf{S}_e \cdot \mathbf{d}_e} (P'_E - P'_P) + \\
&\quad \rho_w^* \frac{\overline{D}[u]_w (S_w^x)^2 + \overline{D}[v]_w (S_w^y)^2}{\mathbf{S}_w \cdot \mathbf{d}_w} (P'_W - P'_P) + \\
&\quad \rho_n^* \frac{\overline{D}[u]_n (S_n^x)^2 + \overline{D}[v]_n (S_n^y)^2}{\mathbf{S}_n \cdot \mathbf{d}_n} (P'_N - P'_P) + \\
&\quad \rho_s^* \frac{\overline{D}[u]_s (S_s^x)^2 + \overline{D}[v]_s (S_s^y)^2}{\mathbf{S}_s \cdot \mathbf{d}_s} (P'_S - P'_P) + \\
&= \Gamma_e^{P'} (P'_E - P'_P) + \Gamma_w^{P'} (P'_W - P'_P) + \Gamma_n^{P'} (P'_N - P'_P) + \Gamma_s^{P'} (P'_S - P'_P) \\
&= -(\Gamma_e^{P'} + \Gamma_w^{P'} + \Gamma_n^{P'} + \Gamma_s^{P'}) P'_P + \Gamma_e^{P'} P'_E + \Gamma_w^{P'} P'_W + \Gamma_n^{P'} P'_N + \Gamma_s^{P'} P'_S
\end{aligned} \tag{76}$$

Moreover, the discretized form of $\Delta[\rho^* \mathbf{U}^*]_P$ is given by Eq. (72). Substituting the various terms in Eq. (71) by their equivalent expressions as derived above, the final form of the pressure-correction equation is:

$$a_P^{P'} P'_P = a_E^{P'} P'_E + a_W^{P'} P'_W + a_N^{P'} P'_N + a_S^{P'} P'_S + b_P^{P'} \tag{77}$$

where

$$\begin{aligned}
a_E^{P'} &= \Gamma_e^{P'} + (C_\rho)_e \parallel -U_e^*, 0 \parallel \\
a_W^{P'} &= \Gamma_w^{P'} + (C_\rho)_w \parallel -U_w^*, 0 \parallel \\
a_N^{P'} &= \Gamma_n^{P'} + (C_\rho)_n \parallel -U_n^*, 0 \parallel \\
a_S^{P'} &= \Gamma_s^{P'} + (C_\rho)_s \parallel -U_s^*, 0 \parallel \\
(a_P^{P'})^\circ &= \frac{\Omega (C_\rho)_P}{\delta t} \\
a_P^{P'} &= a_E^{P'} + a_W^{P'} + a_N^{P'} + a_S^{P'} + (a_P^{P'})^\circ + [(C_\rho)_e U_e^* + (C_\rho)_w U_w^* + (C_\rho)_n U_n^* + (C_\rho)_s U_s^*] \\
b_P^{P'} &= -\frac{(\rho_P - \rho_P^0)}{\delta t} \Omega - ((\rho_e^*)^{\text{HR}} U_e^* + (\rho_w^*)^{\text{HR}} U_w^* + (\rho_n^*)^{\text{HR}} U_n^* + (\rho_s^*)^{\text{HR}} U_s^*)
\end{aligned} \tag{78}$$

OVERALL SOLUTION PROCEDURE

Knowing the solution at time t , the solution at time $t+\delta t$ is obtained as follows:

- Solve implicitly for u and v , using the available pressure and density fields.
- Calculate the D field.
- Solve the pressure correction equation.
- Correct u , v , P and ρ .
- Solve implicitly the energy equation and update the density field.
- Return to the first step and iterate until convergence.

BOUNDARY CONDITIONS

The solutions to the above system of equations require the specification of boundary conditions of which several types are encountered in flow calculations, such as inflow, outflow, and no-flow (impermeable walls, and symmetry lines). Details regarding the various types and their implementation for both incompressible and compressible flow calculations are given below.

INCOMPRESSIBLE FLOWS

Inflow boundary:

At an inflow boundary, the flow enters the computational domain and normally the values of all variables are known. These values can be directly substituted into the discretized equations for the boundary control volumes and thus nothing special needs to be done.

No-flow boundary

At a no-flow boundary, the fluid cannot cross the boundary. Examples of such boundaries are impermeable walls and symmetry lines.

Impermeable wall

For viscous flows, the no-slip condition can be imposed for the velocities at an impermeable wall. According to this condition, the velocity of the fluid at the wall must be equal to the velocity of the wall. For potential flows, the flow at a solid wall is assumed to be totally along the wall. Setting the normal component of velocity to zero imposes this condition. For other scalars, either the scalar value at the wall or its flux may be specified.

Symmetry line

At a symmetry line, the normal component of velocity and the normal gradient of the parallel component of velocity are zero.

$$\mathbf{n} \cdot \mathbf{v} = 0 \quad (79)$$

$$(\mathbf{n} \cdot \nabla) \mathbf{v} = 0 \quad (80)$$

For other scalar variables, both the convective and diffusive fluxes are zero.

These conditions may be expressed as follows:

$$\mathbf{n} \cdot \nabla \phi = 0 \quad (81)$$

In the above expressions, \mathbf{n} is the unit vector normal to the symmetry line.

Outflow boundary

The boundary at which the fluid leaves the computational domain is called an outflow boundary. The most commonly used practice at an outflow boundary is to assume that the diffusive flux is zero and the total flux is purely convective in

nature. This assumption is equivalent to setting the streamwise gradients to zero.

COMPRESSIBLE FLOWS

Inflow boundary

The number of variables that can be specified at the inflow boundary depends on the number of incoming characteristics at that surface. For a two-dimensional subsonic inflow, this requires the specification of three variables. For a supersonic flow, however, all variables must be known a priori. For the case of subsonic inflow there is considerable choice as to which variables are specified. For example, both the velocity components and the temperature may be specified. In internal flows (e.g. flow in nozzles), experimentation with this approach has shown poor convergence characteristics and divergence in the presence of shock waves when HR schemes are used. Better convergence properties are achieved, as described below, by specifying the total conditions (i.e. stagnation temperature and pressure) and the transverse component of velocity or the inlet flow angle. Other variables that are required at the inflow boundary are obtained by extrapolation from the interior.

Prescribed total conditions at inlet

The implementation of this boundary condition, demonstrated at a boundary face f , is accomplished via a technique that incorporates implicitly the influence of pressure on the velocity. For that purpose, the total pressure, total temperature, and flow angle are defined as:

$$P_t = P \left(1 + \frac{\gamma-1}{2} \frac{\mathbf{v} \cdot \mathbf{v}}{\gamma RT} \right)^{\frac{\gamma}{\gamma-1}}, \quad T_t = T \left(1 + \frac{\gamma-1}{2} \frac{\mathbf{v} \cdot \mathbf{v}}{\gamma RT} \right), \quad \tan(\beta) = \frac{v}{u} \quad (82)$$

The procedure can easily be understood by following the sequence of events during a global SIMPLE iteration. The solution process starts by calculating the velocity components at the inlet (f) boundary, u_f and v_f , from equation (82). Then, the momentum equations are solved using u_f and v_f as specified boundary velocities for the current iteration. In calculating the convective flux at the inlet boundary, however, the velocity used is not the one obtained from equation (82) but rather, as described below, it is calculated such that the mass conservation is assured. Having solved the momentum equations, the mass fluxes are updated throughout the solution domain, using the newly calculated velocity field. The new inlet mass fluxes are then evaluated using the velocity components u_f and v_f defined above. Moreover, in deriving the pressure correction equation, the inlet mass flux should include a correction term. In order to avoid any possible negative coefficients in the resulting equation, the correction is applied to the velocity alone, assuming that the density is either prescribed or treated as such within one outer iteration [12,18]. Mathematically, the velocity corrections are expressed via pressure correction as follows:

$$u'_f = \left(\frac{\partial u^*}{\partial P} \right)_f P', \quad v'_f = u'_f \tan(\beta) \quad (83)$$

The coefficient $\left(\frac{\partial u^*}{\partial P} \right)_f$ is obtained from equation (82) as:

$$\left(\frac{\partial u^*}{\partial P} \right)_f = - \frac{\gamma RT^*}{u^* \gamma (1 + \tan^2(\beta)) P_t \left[1 + \frac{\gamma-1}{2} \frac{u^{*2} (1 + \tan^2(\beta))}{\gamma RT^*} \right]^{\frac{1-2\gamma}{\gamma-1}}} \quad (84)$$

The boundary mass flux correction is expressed as a function of the boundary pressure correction as follows:

$$(\rho^* \mathbf{v}')_f \cdot \mathbf{S}_f = \rho_f^* (u'_f S_f^x + v'_f S_f^y) = \rho_f^* \left(\frac{\partial u^*}{\partial P} \right)_f (S_f^x + S_f^y \tan(\beta)) \bar{P}'_f \quad (85)$$

Where \bar{P}'_f is obtained by extrapolating the pressure correction from interior nodes. Thus, the coefficients in the pressure correction equation for the cells next to the boundary are modified accordingly. Once the pressure correction field is obtained the related variables (velocity components, pressure, and density) and the mass fluxes, which are used to calculate the convection fluxes in all equations in the following iteration, are corrected throughout the solution domain, including the inlet boundary. The newly predicted pressure at the inlet boundary is used in equation (82) to calculate new velocities that will serve as the prescribed boundary velocities in the next iteration.

No-flow boundary

The treatment at a no-flow boundary for compressible flows is identical to that for incompressible flows discussed above.

Outflow boundary

Similar to the inflow boundary, the number of variables that can be specified at an outflow boundary is equal to the number of incoming characteristics. For a subsonic outflow, this requires specification of one boundary condition. The most common practice is to assume the static pressure to be known. All other variables are extrapolated from the interior of the computational domain.

Prescribed static pressure

Although the pressure correction at the boundary by definition will be equal to zero the velocity and mass flux corrections will not. Thus, the pressure correction equation needs to be modified for the cells next to the boundary.

The velocity components at the boundary nodes are calculated in a similar way as in equation (55), namely,

$$\mathbf{v}_f^* = \overline{\mathbf{H}}[\mathbf{v}]_f - \overline{\mathbf{D}}_f(\nabla P)_f \quad (86)$$

which results in the following expressions for the velocity corrections:

$$\mathbf{v}'_f = -\overline{\mathbf{D}}_f(\overline{\nabla P'})_f \quad (87)$$

The mass flux correction is calculated as:

$$\begin{aligned} (\rho^* \overline{\mathbf{v}'} + \rho' \overline{\mathbf{v}^*})_f \cdot \mathbf{S}_f &= \rho^* (-\overline{\mathbf{D}}_f(\nabla P')_f \cdot \mathbf{S}_f) + C_\rho \overline{P'_f} \overline{U'_f} \\ &= -\rho^* \frac{\overline{D}[u]_f (S_f^x)^2 + \overline{D}[v]_f (S_f^y)^2}{S_f^x d_f^x + S_f^y d_f^y} (\overline{P'_f} - P'_f) + C_\rho \overline{P'_f} \overline{U'_f} \end{aligned} \quad (88)$$

The resulting modifications for the coefficients of interior nodes in the pressure correction equation are easily derived from the above expression. The flux velocity correction U'_f at the boundary is obtained, after solving the pressure-correction equation, from the following formula:

$$U'_f = -\frac{\overline{D}[u]_f (S_f^x)^2 + \overline{D}[v]_f (S_f^y)^2}{S_f^x d_f^x + S_f^y d_f^y} (\overline{P'_f} - P'_f) - \left(\overline{D}[u]_f (\overline{\nabla P'})_f^x \kappa_f^x + \overline{D}[v]_f (\overline{\nabla P'})_f^y \kappa_f^y \right) \quad (89)$$

In the previous equations, the overbar denotes values which are obtained by extrapolation. Moreover, the above procedure is equally applicable to incompressible flows and the corresponding expressions for the velocities and mass fluxes at boundaries can be derived from those given above by setting the density correction to zero.

For a supersonic outflow, all variables must be determined by extrapolation. The velocity and mass flux, as well as their corrections are obtained in the same way explained above. However, since the pressure is not known, the pressure correction at the boundary node, P'_F , is not zero. Thus, it should be expressed in terms of the values at interior nodes and the coefficients of the pressure correction equation for the next-to-boundary cells must be modified accordingly.

RESULTS AND DISCUSSION

The validity of the above described solution procedure is demonstrated in this section by presenting solutions to the following four inviscid test cases: (i) flow in a converging diverging nozzle; (ii) flow over a bump; (iii) supersonic flow over a step; and (iv) the unsteady duct filling problem.

FLOW IN A CONVERGING-DIVERGING NOZZLE

The first test selected is a standard one that has been used by several researchers for comparison purposes [18,19]. The problem is first solved using a pseudo-one-dimensional variable area code. The cross-sectional area of the nozzle varies as

$$S_{(x)} = S_{th} + (S_i - S_{th}) \left(1 - \frac{x}{5}\right)^2 \quad (90)$$

where $S_i=2.035$ and $S_{th}=1$ are the inlet and throat areas, respectively, and $0 \leq x \leq 10$. Solutions are obtained over a wide range of inlet Mach numbers ranging from the incompressible limit ($M=0.1$) to supersonic ($M=7$), passing through

transonic and including strong normal shock waves.

At all Mach number values, two sets of results are generated and compared against the exact analytical solution. The first is obtained using the third-order SMART scheme [2] for all variables except density (for which the UPWIND [21] scheme is used). In the second set however, the SMART scheme is used for all variables including density. Results displayed in Figs. 4, 5, and 6 are for inlet Mach numbers of 0.1, 0.3, and 7, respectively. In all three figures, results are displayed for four different uniform grid networks of sizes 125, 79, 59, and 39 control volumes. As expected, results shown in Fig. 4 ($M_{in}=0.1$, subsonic throughout) reveal a decrease in accuracy as the grid density decreases. In addition, for all grid sizes, the solution is nearly insensitive to using a HR scheme when interpolating for density. This is expected, since for this inlet Mach number value, variations in density are small and the flow can be considered to be nearly incompressible. For $M_{in}=0.3$ (Fig. 5), the backpressure is chosen such that a supersonic flow is obtained in the diverging section (i.e. $M_{th}=1$, transonic). The Mach number distributions after the throat are depicted in Fig. 5. As shown, the use of a HR scheme for interpolating the values of density at the control volume faces improves predictions. This improvement decreases with increasing grid density. However, except for the value near the exit section, results predicted with values of density at the control volume faces calculated using a HR scheme are nearly coincident with the exact solution even for the coarsest grid tested (see Fig. 5(d)). The Mach number distributions depicted in Fig. 6 are for a fully supersonic flow in the nozzle. The trend of results is similar to that of Fig. 5. Again important improvements are

obtained when using the SMART scheme for density interpolation.

The accuracy of the new technique in predicting normal shock waves is revealed by the Mach number and pressure distributions displayed in Figs. 7(a) and 7(b), respectively. Two backpressure values that cause normal shock waves at $x=7$ and 9 are used. For each back pressure, three different solutions (one using the UPWIND scheme for all variables; the second one using the SMART scheme for all variables; the third one using the SMART scheme for all variables except density for which the UPWIND scheme is used) are obtained and compared against the exact solution. All solutions are obtained by subdividing the domain into 121 uniform control volumes. As shown, predictions obtained using the UPWIND scheme for all variables are very smooth but highly diffusive and cause a smearing in the shock wave. Results obtained using the SMART scheme for all variables except density are more accurate than those obtained with the UPWIND scheme and cause less smearing in the shock waves. The best results are, however, obtained when employing the SMART scheme for all variables including density. The plots also reveal that solutions obtained using the SMART scheme show some oscillations behind the shock. This is a feature of all HR schemes. The oscillations are usually centered on the accurate solution and are reduced with grid refinement in both wavelength and amplitude.

As a further check on the applicability of the new technique in the subsonic, transonic, and supersonic regimes, results are generated for several inlet Mach number values $0.1 \leq M_{in} \leq 7$ and displayed in Fig. 8. As shown, the Mach number and pressure distributions are in excellent agreement with the exact solution.

Two-dimensional predictions for some of the above-presented cases were generated with 100x15 mesh covering one half of the nozzle. The resultant area-averaged variations of Mach number are depicted in Fig. 9. Results were obtained using the SMART scheme for all variables including density. As for the quasi-one-dimensional predictions, results are in excellent agreement with the exact solutions.

FLOW OVER A CIRCULAR ARC BUMP

The physical situation consists of a channel of width equal to the length of the circular arc bump and of total length equal to three lengths of the bump. This problem has been used by many researchers [18,19,23] to test the accuracy and stability of numerical algorithms. Results are presented for three different types of flow (subsonic, transonic, and supersonic). For subsonic and transonic calculations, the thickness-to-chord ratio is 10% and for supersonic flow calculations it is 4%. In all flow regimes, predictions obtained over a relatively coarse grid using the SMART scheme for all variables including density are compared against results obtained over the same grid using the SMART scheme for all variables except density, for which the UPWIND scheme is used. Due to the unavailability of an exact solution to the problem, a solution using a dense grid is generated and treated as the most accurate solution against which coarse grid results are compared.

Subsonic flow over a circular arc bump

With an inlet Mach number of 0.5, the inviscid flow in the channel is fully subsonic and symmetric across the middle of the bump. At the inlet, the flow is

assumed to have uniform properties and all variables, except pressure, are specified. At the outlet section, the pressure is prescribed and all other variables are extrapolated from the interior of the domain. The flow tangency condition is applied at the walls. As shown in Fig. 10(a), the physical domain is non-uniformly decomposed into 63×16 control volumes. The dense grid solution is obtained over a mesh of size 252×54 control volumes. Isobars displayed in Fig. 10(b) reveal that the coarse grid solution obtained with the SMART scheme for all variables falls on top of the dense grid solution. The use of the upwind scheme for density however, lowers the overall solution accuracy. The same conclusion can be drawn when comparing the Mach number distribution along the lower and upper walls of the channel. As seen in Fig. 10(c), the coarse grid profile obtained using the SMART scheme for density is closer to the dense grid profile than the one predicted employing the upwind scheme for density. The difference in results between the coarse grid solutions is not large for this test case. This is expected since the flow is subsonic and variations in density are relatively small. Larger differences are anticipated in the transonic and supersonic regimes.

Transonic flow over a circular arc bump

With the exception of the inlet Mach number being set to 0.675, the grid distribution and the implementation of boundary conditions are identical to those described for subsonic flow. Results are displayed in Fig. 11 in terms of isobars and Mach profiles along the walls. In Fig. 11(a) isobars generated using a dense grid and the SMART scheme for all variables are displayed. Fig. 11(b) presents a comparison between the coarse grid and dense grid results. As

shown, the use of the HR SMART scheme for density greatly improves the predictions. Isobars generated over a coarse grid (63x16 c.v.) using the SMART scheme for all variables are very close to the ones obtained with a dense grid (252x54 c.v.). This is in difference with coarse grid results obtained using the upwind scheme for density and the SMART scheme for all other variables, which noticeably deviate from the dense grid solution. This is further apparent in Fig. 11(c) where Mach number profiles along the lower and upper walls are compared. As shown, the most accurate coarse grid results are those obtained with the SMART scheme for all variables and the worst ones are achieved with the upwind scheme for all variables. The maximum Mach number along the lower wall ($\cong 1.41$), predicted with a dense grid, is in excellent agreement with published values [18,19,23]. The use of a HR scheme for density greatly enhances the solution accuracy with coarse grid profiles generated using the SMART scheme for all variables being very close to the dense grid results. By comparing coarse grid profiles along the lower wall, the all-SMART solution is about 11% more accurate than the solution obtained using SMART for all variables and upwind for density and 21% more accurate than the highly diffusive all-upwind solution.

Supersonic flow over a circular arc bump

Computations are presented for two inlet Mach number values of 1.4 and 1.65. For these values of inlet Mach number and for the used geometry, the flow is also supersonic at the outlet. Thus, all variables at inlet are prescribed, and at outlet all variables are extrapolated. For $M_{in}=1.4$, results are presented in Figs. 12 and 13. The coarse grid used is displayed in Fig. 12(a). Mach number

contours are compared in Fig. 12(b). As before, the coarse grid all-SMART results (58x18 c.v.), being closer to the dense grid results (158x78 c.v.), are more accurate than those obtained when using the upwind scheme for density. The fine grid Mach contours are displayed in Fig. 12(c). As depicted, the reflection and intersection of the shocks is very well resolved without undue oscillations. The Mach profiles along the lower and upper walls, depicted in Fig. 12(d), are in excellent agreement with published results [56] and reveal good enhancement in accuracy when using the SMART scheme for evaluating interface density values. The use of the upwind scheme to compute density deteriorates the solution accuracy even though a HR scheme is used for other variables. The all-upwind results are highly diffusive. Finally, results for this case were obtained over a grid of 90x30 nodes, of which 80x30 were uniformly distributed in the region downstream of the bump's leading corner. Resulting Mach contours are compared in Fig. 13 with four other solutions [19,57,58] using the same grid density. The comparison demonstrates the credibility and superiority of the current solution methodology. The wiggles and oscillations in some regions around the shock waves in the published solutions are not present in the newly predicted one.

For $M_{in}=1.65$, results are depicted in Fig. 14. The coarse grid used is shown in Fig. 14(a) and the Mach contours are compared in Fig. 14(b). The trend of results is consistent with what was obtained earlier. Fine grid results displayed in Figs. 14(c) and 14(d) are in excellent agreement with published results [18,23]. The Mach contours in Fig. 14(c) are very smooth and do not show any sign of oscillations. The profiles along the lower and upper walls indicate once

more that the use of a HR scheme for density increases the solution accuracy. Thus, for subsonic, transonic, and supersonic flows the use of a HR scheme for calculating interface density values undoubtedly increases the solution accuracy.

SUPERSONIC FLOW OVER A STEP

The physical situation and boundary conditions for the problem are depicted in Fig. 15(a). The problem was first solved using the upwind scheme and the predicted isobars are depicted in Fig. 15(b). In fig. 15(c), the isobars reported in [17] are presented. As shown, the current predictions fall on top of the ones reported by Marchi and Maliska [17] eliminating any doubts about the correctness of the implementation of the solution algorithm and boundary conditions. The isobars resulting from a dense grid solution (23x108 c.v.) using the upwind scheme for all variables are presented in Fig. 16(a). The effectiveness of using a HR scheme for density is demonstrated through the comparison depicted in Fig. 16(b). Two different isobars representing pressure ratios of values 0.9 and 2.5 are considered. Solutions obtained over a coarse grid (38x36 c.v.) using: (i) the SMART schemes for all variables, (ii) the SMART scheme for all variables except density and the upwind scheme for density, and (iii) the upwind scheme for all variables, are compared against a dense grid solution (238x108 c.v.) generated using the upwind scheme for all variables. Once more the virtues of using a HR scheme for density is obvious. The coarse grid isobars obtained using the SMART scheme for all variables, being nearly coincident with dense grid isobars, are remarkably more accurate than coarse grid results obtained using the SMART scheme for all variables except density

and the upwind scheme for density. Finally, in order to show that the suggested solution algorithm is applicable to all HR schemes, the same problem was solved over a coarse grid using a number of HR schemes and results are displayed in Fig. 17. All results exhibit the same behavior and are by far more accurate than the solution obtained with the upwind scheme reported in the literature [17,59].

IDEAL UNSTEADY DUCT FILLING

Having established the credibility of the solution method, an unsteady process of duct filling is considered. The physical situation for the problem consists of a duct containing a gas ($\gamma=1.4$) that is isentropically expanded from atmospheric pressure. The duct is considered to be frictionless, adiabatic, and of constant cross-section. Moreover, it is assumed that the duct is opened instantaneously to the surrounding atmosphere, inflow is isentropic, and in the fully open state the effective flow area at the duct end is equal to the duct cross-sectional area. The unsteady one-dimensional duct filling process is solved using a two-dimensional code over a uniform grid of density 299×3 control volumes, a time step of value 10^{-4} , and the SMART scheme for all variables.

The problem is solved for a surrounding to duct pressure ratio of 2.45 and generated results are displayed in Fig. 18. Due to the lower pressure of the gas contained in the duct, when the duct end is suddenly opened, a compression wave is established instantly as a shock wave. The wave diagram for the process is shown in Fig. 18(a). The shock wave moves in the duct until the closed end is reached. On reaching the closed end, the compression wave is reflected and the duct filling process continues until the reflected shock wave is

at the open end. Beyond that, duct emptying starts and computations were stopped at that moment in time. In addition, the path of the first particle to enter the duct is shown in the figure. This was computed by storing the duct velocities at all time steps and then integrating in time to locate the position of the particle. Results depicted in Fig. 18(a) were compared against similar ones reported by Azoury [60] using a graphical method. The two sets of results were found to be in excellent agreement with the ones computed here falling right on top of those reported.

The variation of Mach number with time at the open end of the duct is displayed in Fig. 18(b). With the exception of the slight overshoot at the beginning of the computations, the Mach number remains constant throughout the filling process and it instantaneously decreases to zero at the time when the reflected shock wave reaches the open end of the duct. When using the same reference quantities, the analytical solution to the problem reported in [60] predicts a constant Mach number of value 0.4391 which is 0.21% different than the one obtained here. Moreover, the instantaneous decrease of Mach number to zero is well predicted by the method. Finally, the increase in mass within the duct is presented in Fig. 18(c). As expected, due to the constant value of the inlet Mach number the mass increases linearly with time.

CONCLUDING REMARKS

A new collocated high-resolution pressure-based algorithm for the solution of fluid flow at all speeds was formulated. The new features in the algorithm are the use of a HR scheme in calculating the density values at the control volume

faces and the use of the NVSF methodology for bounding the convection fluxes. The method was tested by solving four problems representing flow in a converging-diverging nozzle, flow over a bump, flow over an obstacle, and unsteady duct filling. Mach number values spanning the entire subsonic to supersonic spectrum, including transonic flows with strong normal shock waves, were considered. In all cases, results obtained were very promising and revealed good enhancement in accuracy at high Mach number values when calculating interface density values using a High-Resolution scheme.

ACKNOWLEDGMENTS

Thanks are due to Prof. P.H. Azoury for reviewing the manuscript and for the valuable discussions the authors had with him during the various phases of the work. This work was supported by the European Office of Aerospace Research and Development (EOARD) through contract SPC-99-4003.

FIGURE CAPTIONS

Fig. 1 Control Volume.

Fig. 2 Typical control volume faces and geometric nomenclature.

Fig. 3 (a) Control volume nodes; (b) Normalization; (c) CBC Criterion.

Fig. 4 Comparison of Mach number variation for an inlet Mach number of 0.1.

Fig. 5 Comparison of Mach number variation for an inlet Mach number of 0.3.

Fig. 6 Comparison of Mach number variation for an inlet Mach number of 7.

Fig. 7 Transonic inviscid flow in a converging-diverging nozzle: (a) Mach number distributions, (b) pressure distributions.

Fig. 8 Comparison of (a) Mach number and (b) pressure distributions for one-dimensional inviscid nozzle flow.

Fig. 9 Comparison of distributions of (a) area-averaged Mach number and (b) pressure for inviscid nozzle flow from 2-D solution.

Fig. 10 Subsonic flow over a 10% circular bump; (a) coarse grid used, (b) isobars, and (c) profiles along the walls.

Fig. 11 Transonic flow over a 10% circular bump; (a) Isobars using a dense grid, (b) isobars using various schemes, and (c) profiles along the

walls.

Fig. 12 Supersonic flow over a 4% circular bump ($M_{in}=1.4$); (a) coarse grid used, (b) Mach number contours using various schemes, (c) Mach number contours using a dense grid, and (d) profiles along the walls.

Fig. 13 Supersonic inviscid flow over 4% bump ($M_{in}=1.4$): Mach-number contours.

Fig. 14 Supersonic flow over a 4% circular bump ($M_{in}=1.65$); (a) coarse grid used, (b) Mach number contours using various schemes, (c) Mach number contours using a dense grid, and (d) profiles along the walls.

Fig. 15 Supersonic flow over an obstacle: (a) Physical situation, (b) Isobars using the upwind scheme (40X38 grid points), and (c) results obtained by Marchi and Maliska using (44x36 grid points).

Fig. 16 Supersonic flow over an obstacle: (a) Isobars generated using a dense grid; (b) Isobars generated using different schemes for supersonic flow over an obstacle.

Fig. 17 Isobars for the flow over an obstacle obtained from different HR schemes.

Fig. 18 (a) Wave diagram for optimum duct-filling process; (b) Mach number distribution at inflow; (c) Variation of mass with time.

REFERENCES

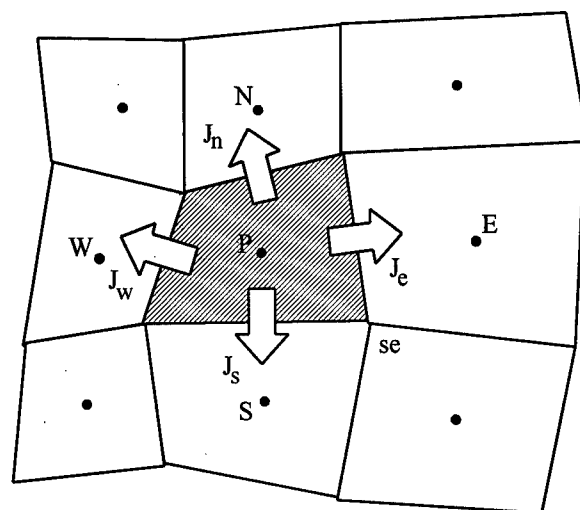
- 1 Patankar, S.V., Numerical Heat Transfer and Fluid Flow, Hemisphere, N.Y., 1981.
- 2 Darwish, M. and Moukalled, F., "A new Route for Building Bounded Skew-Upwind Schemes," Computer Methods in Applied Mechanics and Engineering, vol. 129, pp. 221-233, 1996.
- 3 Moukalled, F. and Darwish, M., "A New Bounded Skew Central Difference Scheme, Part I. Formulation and testing," Numerical Heat Transfer, Part B, Vol. 31, No. 1, pp. 91-110, 1997.
- 4 Moukalled, F. and Darwish, M., "A New Family of Streamline-Based Very High Resolution Schemes," Numerical Heat Transfer, vol. 32, No. 3, pp. 299-320, 1997.
- 5 Darwish, M. and Moukalled, F., "An Efficient Very High-Resolution scheme Based on an Adaptive-Scheme Strategy," Numerical Heat Transfer, Part B, vol. 34, pp. 191-213, 1998.
- 6 Moukalled, F. and Darwish, M., "New Family of Adaptive Very High Resolution Schemes," Numerical Heat Transfer, Part B, vol. 34, pp. 215-239, 1998.
- 7 Zhu, J. and Rodi, W., "A Low Dispersion and Bounded Convection Scheme," Comp. Meth. Appl. Mech. & Eng., vol. 92, pp. 897-906, 1991.
- 8 Gaskell, P.H. and Lau, A.K.C., "Curvature compensated Convective Transport: SMART, a new boundedness preserving transport algorithm," Int. J. Num. Meth. Fluids, vol. 8, pp. 617-641, 1988.
- 9 Zhu, J., "A Low-Diffusive and Oscillation-Free Convection Scheme," Comm. Appl. Num. Meth., vol. 7, pp. 225-232, 1991.
- 10 Lin., H. and Chieng, C.C., "Characteristic-Based Flux Limiters of an Essentially Third-Order Flux-Splitting Method for Hyperbolic Conservation Laws," Int. J. Num. Meth. Fluids, vol. 13, pp. 287-307, 1991.
- 11 Darwish, M.S., "A new High-Resolution Scheme Based on the Normalized Variable Formulation," Numerical Heat Transfer, Part B: Fundamentals, vol. 24, pp. 353-371, 1993.
- 12 Karki, K.C., "A Calculation Procedure for Viscous Flows at All Speeds in Complex Geometries," Ph.D. Thesis, University of Minnesota, June 1986.
- 13 Shyy, W. and Braaten, M.E., "Adaptive Grid Computation for Inviscid Compressible Flows Using a Pressure Correction Method," AIAA Paper 88-3566-CP, 1988.
- 14 Shyy, W. and Chen, M.H., "Pressure-Based Multigrid Algorithm for Flow at

- All Speeds," *AIAA Journal*, vol. 30, no. 11, pp. 2660-2669, 1992.
- 15 Rhie, C.M., "A Pressure Based Navier-Stokes Solver Using the Multigrid Method," *AIAA paper* 86-0207, 1986.
 - 16 Yang, H.Q., Habchi, S.D., and Przekwas, A.J., "General Strong Conservation Formulation of Navier-Stokes Equations in Non-orthogonal Curvilinear Coordinates," *AIAA Journal*, vol. 32, no. 5, pp. 936-941, 1994.
 - 17 Marchi, C.H. and Maliska, C.R., "A Non-orthogonal Finite-Volume Methods for the Solution of All Speed Flows Using Co-Located Variables," *Numerical Heat Transfer, Part B*, vol. 26, pp. 293-311, 1994.
 - 18 Demirdzic, I., Lilek, Z., and Peric, M., "A Collocated Finite Volume Method For Predicting Flows at All Speeds," *International Journal for Numerical Methods in Fluids*, vol. 16, pp. 1029-1050, 1993.
 - 19 Lien, F.S. and Leschziner, M.A., "A Pressure-Velocity Solution Strategy for Compressible Flow and Its Application to Shock/Boundary-Layer Interaction Using Second-Moment Turbulence Closure," *Journal of Fluids Engineering*, vol. 115, pp. 717-725, 1993.
 - 20 Lien, F.S. and Leschziner, M.A., "A General Non-Orthogonal Collocated Finite Volume Algorithm for Turbulent Flow at All Speeds Incorporating Second-Moment Turbulence-Transport Closure, Part 1: Computational Implementation," *Comput. Methods Appl. Mech. Engrg.*, vol. 114, pp. 123-148, 1994.
 - 21 Politis, E.S. and Giannakoglou, K.C., "A Pressure-Based Algorithm for High-Speed Turbomachinery Flows," *International Journal for Numerical Methods in Fluids*, vol. 25, pp. 63-80, 1997.
 - 22 Chen, K.H. and Pletcher, R.H., "Primitive Variable, Strongly Implicit Calculation Procedure for Viscous Flows at All Speeds," *AIAA Journal*, vol. 29, no. 8, pp. 1241-1249, 1991.
 - 23 Karimian, S.M.H. and Schneider, G.E., "Pressure-Based Control-Volume Finite Element Method for Flow at All Speeds," *AIAA Journal*, vol. 33, no. 9, pp. 1611-1618, 1995.
 - 24 Leonard, B.P., "Locally Modified Quick Scheme for Highly Convective 2-D and 3-D Flows," Taylor, C. and Morgan, K. (eds.), *Numerical Methods in Laminar and Turbulent Flows*, Pineridge Press, Swansea, U.K., vol. 15, pp. 35-47, 1987.
 - 25 Darwish, M.S. and Moukalled, F., "Normalized Variable and Space Formulation Methodology For High-Resolution Schemes," *Numerical Heat Transfer, Part B*, vol. 26, pp. 79-96, 1994.
 - 26 Harten, A., "High Resolution Schemes for Hyperbolic Conservation Laws," *Journal of Computational Physics*, vol. 49, no. 3, pp. 357-393, 1983.
 - 27 Zwart, P.J., Raithby, G.D., and Raw, M.J., "An integrated Space-Time Finite-Volume Method for Moving-Boundary Problems," *Numerical Heat*

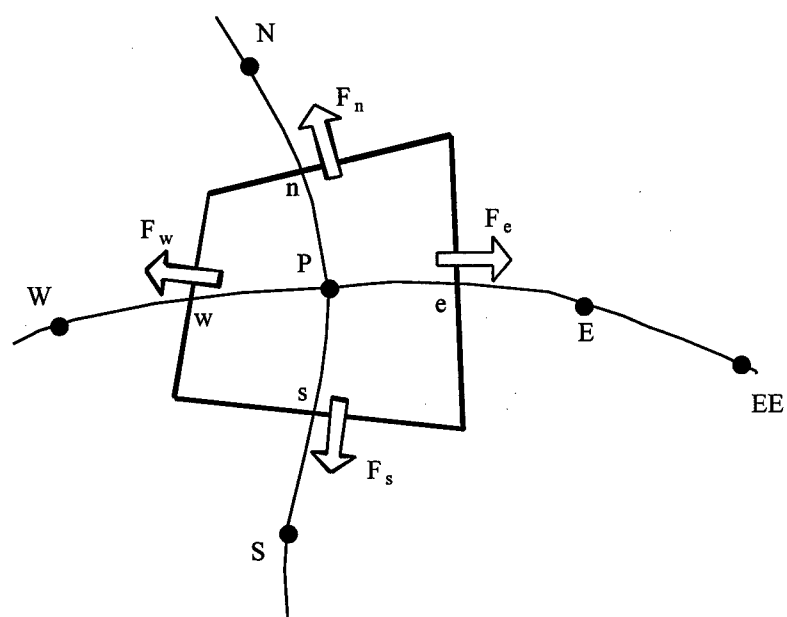
- Transfer Part B, vol. 34, pp. 257-270, 1998.
- 28 Ferziger, J.H. and Peric, M., *Computational Methods for Fluid Dynamics*, pp. 217-222, Springer-Verlag, Berlin, 1996.
 - 29 Rubin, S.G. and Khosla, P.K., "Polynomial Interpolation Method for Viscous Flow Calculations," *Journal of Computational Physics*, vol. 27, pp. 153-168, 1982.
 - 30 Darwish, M. and Moukalled, F., "The Normalized Weighting Factor Method: A Novel Technique for Accelerating the Convergence of High-Resolution Convective Schemes," *Numerical Heat Transfer, Part B, Vol. 30, No. 2*, pp. 217-237, 1996.
 - 31 Adams, L. and Jordan, H., "Is SOR Color-Blind?," *SIAM J. Sci. Statist. Comput.*, vol. 7, pp. 490-506, 1986.
 - 32 Stone, H.L., "Iterative Solution of Implicit Approximations of Multidimensional Partial Differential Equations," *SIAM J. Numer. Anal.*, vol. 5, No. 3, pp. 530-558, 1968.
 - 33 Kershaw, D., "The Incomplete Cholesky-Conjugate Gradient Method for The Iterative Solution of Systems of Linear Equations," *Journal of Computational Physics*, vol. 26, pp. 43-65, 1978.
 - 34 Brandt, A., "Multi-Level Adaptive Solutions to Boundary-Value Problems," *Math. Comp.*, vol. 31, pp. 333-390, 1977.
 - 35 Thomas, L.H., "Elliptic Problems in Linear Difference Equations over a Network," *Watson Sci. Comput. Lab. Report*, Columbia University, New York.
 - 36 Zalesak, S.T., "Fully Multidimensional Flux-Corrected Transport Algorithm for Fluids," *Journal of Computational Physics*, vol. 31, pp. 335-362, 1979.
 - 37 Chapman, M., "FRAM Nonlinear Damping Algorithm for the Continuity Equation," *Journal of Computational Physics*, vol. 44, pp. 84-103, 1981.
 - 38 Peric, M., *A Finite Volume Method for the Prediction of Three Dimensional Fluid Flow in Complex Ducts*, Ph.D. Thesis, Imperial College, Mechanical Engineering Department, London, 1985.
 - 39 Zhu, J. and Leschziner, M.A., "A Local Oscillation-Damping Algorithm for Higher Order Convection Schemes," *Computer Methods in Applied Mechanics and Engineering*, vol. 67, pp. 355-366, 1988.
 - 40 Leonard, B.P., "Simple High-Accuracy Resolution Program for Convective Modelling of Discontinuities," *International Journal for Numerical Methods in Engineering*, vol. 8, pp. 1291-1318, 1988.
 - 41 Chakravarthy, S.R. and Osher, S., "High Resolution Applications of the OSHER Upwind Scheme for the Euler Equations," *AIAA Paper 83-1943*, 1983.

- 42 Van Leer, B., "Towards the Ultimate Conservative Difference Scheme. V. A Second-Order Sequel to Godunov's Method," *Journal of Computational Physics*, vol. 23, pp. 101-136, 1977.
- 43 Van Leer, B., "Towards the Ultimate Conservative Difference Scheme. II. Monotonicity and Conservation Combined in a Second Order Scheme," *Journal of Computational Physics*, vol. 14, pp. 361-370, 1974.
- 44 Leonard, B.P., "The ULTIMATE Conservative Difference Scheme Applied to Unsteady one-dimensional Advection," *Computer Methods in Applied Mechanics and Engineering*, vol. 88, pp. 17-74, 1991.
- 45 Zijlema, M., "On The Construction of a Third-Order Accurate Monotone Convection Scheme with Application to Turbulent Flows in General Domains," *International Journal for Numerical Methods in Fluids*, vol. 22, pp. 619-641, 1996.
- 46 Patankar, S.V. and Spalding, D.B., "A Calculation Procedure for Heat, Mass and Momentum Transfer in three-dimensional Parabolic Flows," *International Journal of Heat and Mass Transfer*, vol. 15, pp. 1787-1806, 1972.
- 47 Van Doormaal, J. P. and Raithby, G. D. "Enhancement of the SIMPLE Method for Predicting Incompressible Fluid Flows" *Numerical Heat Transfer*, vol. 7, pp. 147-163, 1984.
- 48 Maliska, C.R. and Raithby, G.D., "Calculating 3-D fluid Flows Using non-orthogonal Grid," *Proc. Third Int. Conf. on Numerical Methods in Laminar and Turbulent Flows*, Seattle, pp. 656-666, 1983.
- 49 Issa, R.I., "Solution of the Implicit Discretized Fluid Flow Equations by Operator Splitting," *Mechanical Engineering Report*, FS/82/15, Imperial College, London, 1982.
- 50 Van Doormaal, J. P. and Raithby, G. D. "An Evaluation of the Segregated Approach for Predicting Incompressible Fluid Flows," *ASME Paper 85-HT-9*, Presented at the National Heat Transfer Conference, Denver, Colorado, August 4-7, 1985.
- 51 Acharya, S., and Moukalled, F., "Improvements to Incompressible Flow Calculation on a Non-Staggered Curvilinear Grid," *Numerical Heat Transfer, Part B*, vol. 15, pp. 131-152, 1989.
- 52 Spalding D. B. 'Mathematical Modeling of Fluid Mechanics, Heat Transfer and Mass Transfer Processes,' *Mech. Eng. Dept., Report HTS/80/1*, Imperial College of Science, Technology and Medicine, London, 1980.
- 53 Moukalled, F. and Darwish, M., "A Unified Formulation of the Segregated Class of Algorithms for Fluid Flow at All Speeds," *Numerical Heat Transfer, Part B*, (in press).
- 54 Rhie, C.M., *A Numerical Study of the Flow Past an Isolated Airfoil with Separation*, Ph.D. Thesis, Department of Mechanical and Industrial Engineering, University of Illinois at Urbana-Champaign, 1981.

- 55 Majumdar, S. "Role of Under-relaxation in Momentum Interpolation For Calculation of Flow With Non-staggered Grids," Numerical Heat Transfer, Vol. 13, pp. 125-132, 1988.
- 56 Ni, R.H., "A Multiple Grid Scheme for Solving the Euler Equation," AIAA Journal, vol. 20, pp. 1565-1571, 1982.
- 57 Dimitriadis, K.P., and Leschziner, M.A., 1991, "A cell-Vertex TVD Scheme for Transonic Viscous Flow," Numerical Methods in Laminar and Turbulent Flow, vol. 7, C. Taylor, J.H. Chin and G.M. Homsy, eds, pp. 874-885, 1991.
- 58 Stolcis, L., and Johnston, L.J., "Solution of the Euler Equation on Unstructured Grid for Two-Dimensional Compressible Flow," The Aeronautical Journal, vol. 94, pp. 181-195, 1990.
- 59 Van Doormaal, J.P., "Numerical Methods for the solution of Compressible and Incompressible Flows," Ph.D. thesis, University of Waterloo, Waterloo, Ont., Canada, 1985.
- 60 Azoury, P.H., "Engineering Applications of Unsteady Fluid Flow," John Wiley & Sons, 1992.

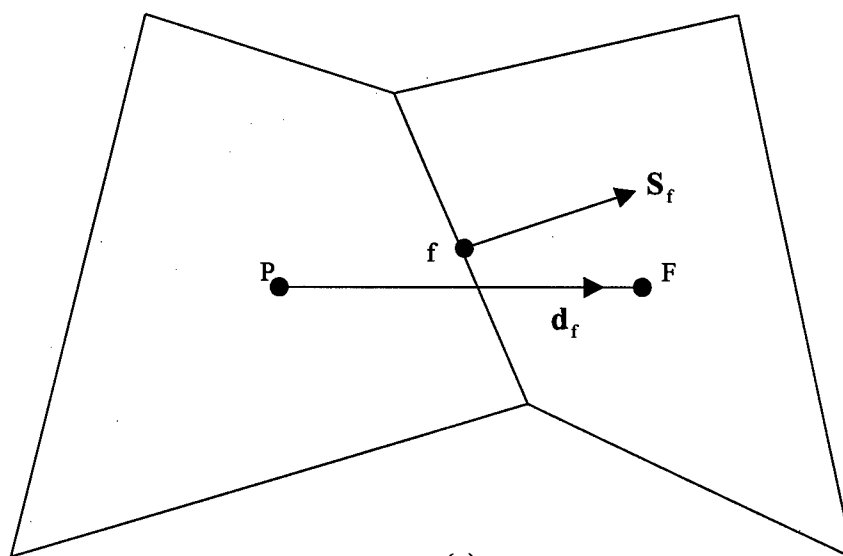


(a)

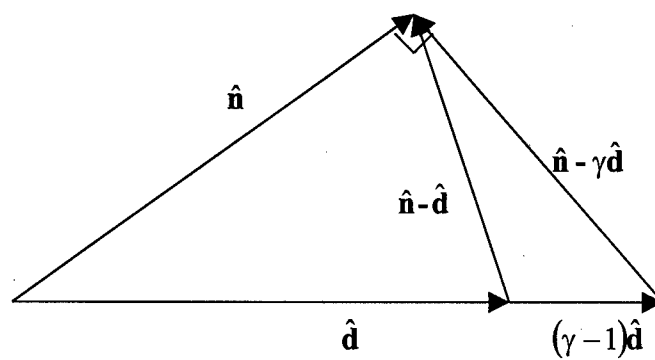


(b)

Fig. 1 Control Volume.

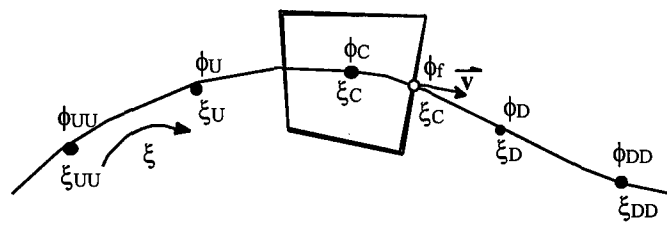


(a)

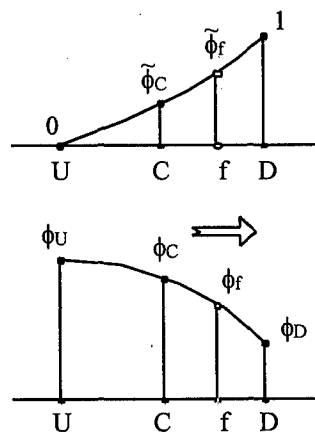


(b)

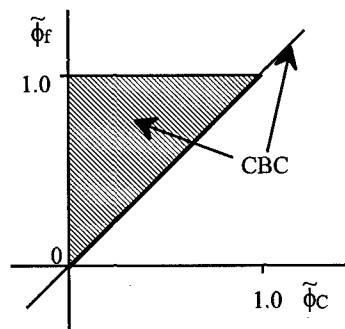
Fig. 2 Typical control volume faces and geometric nomenclature.



(a)

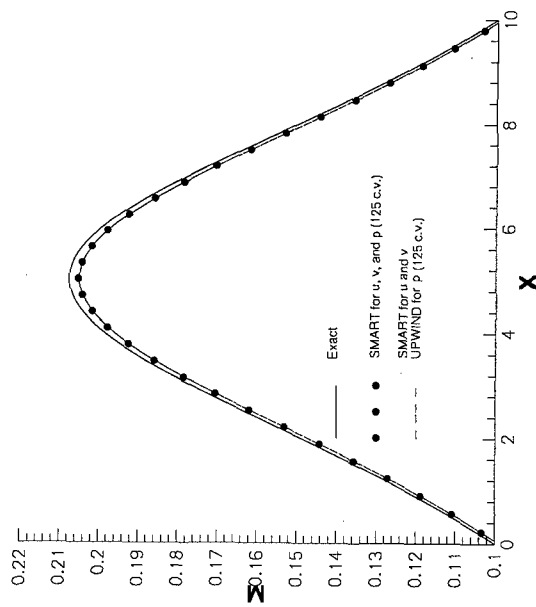


(b)

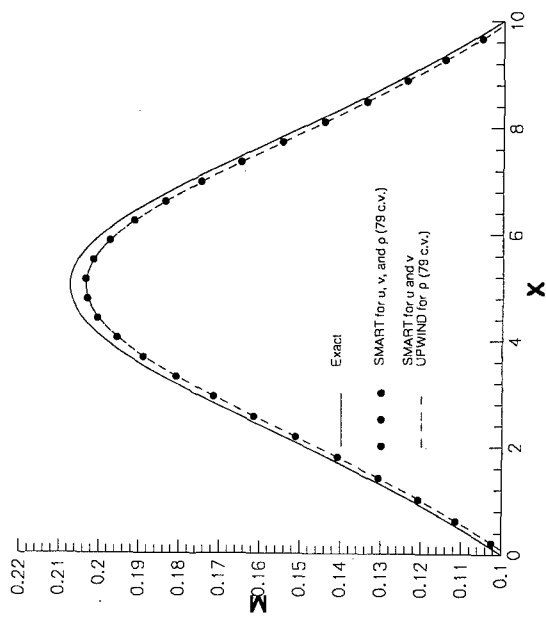


(c)

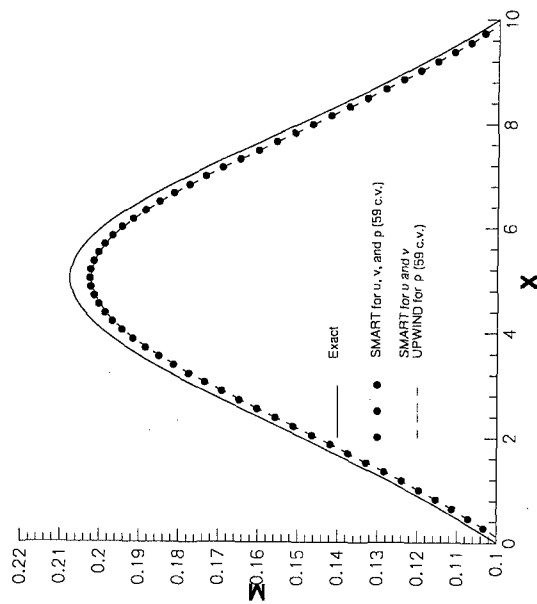
Fig. 3 (a) Control volume nodes; (b) Normalization; (c) CBC Criterion.



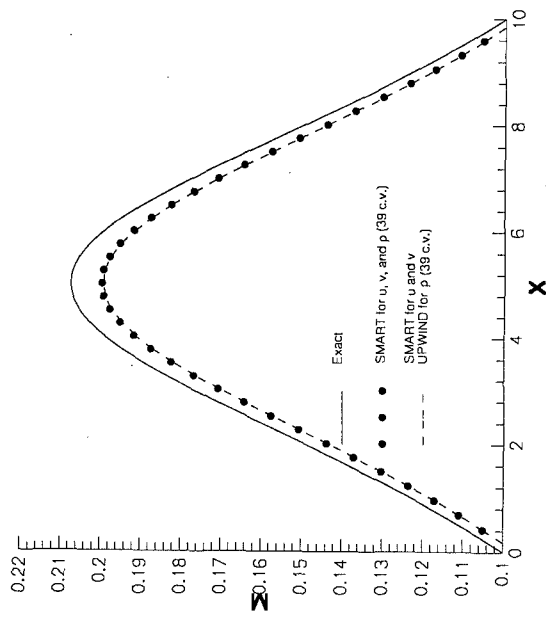
(a)



(b)

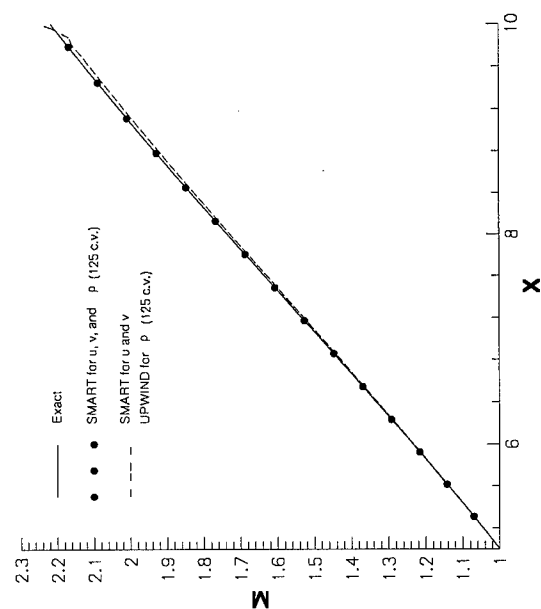


(c)

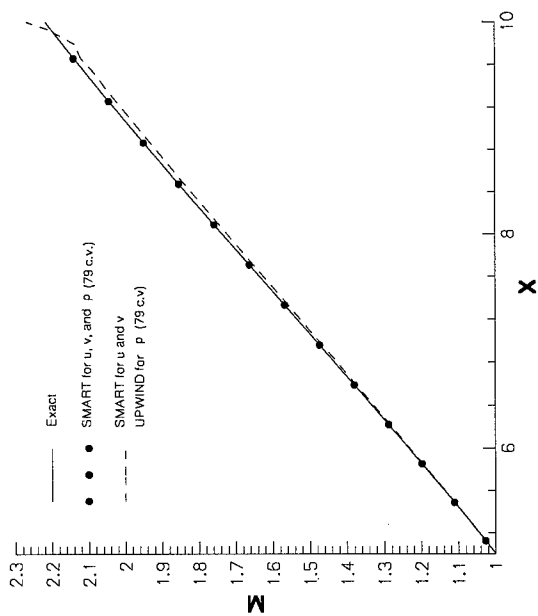


(d)

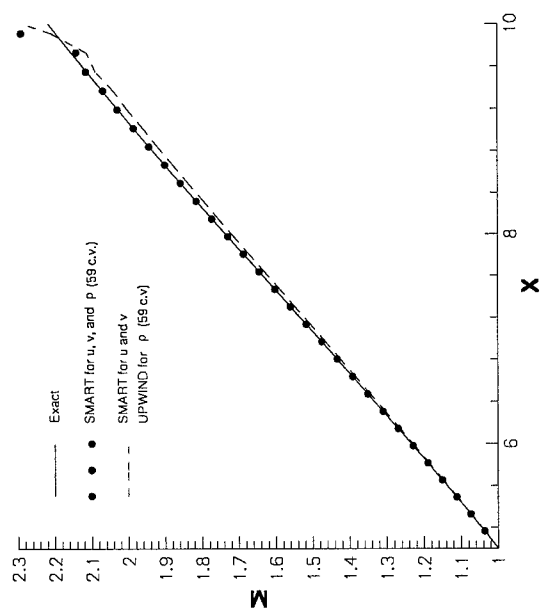
Fig. 4 Comparison of Mach number variation for an inlet Mach number of 0.1.



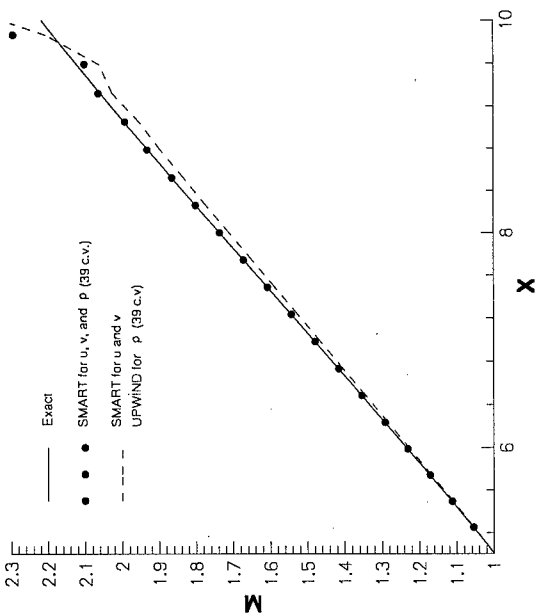
(a)



(b)

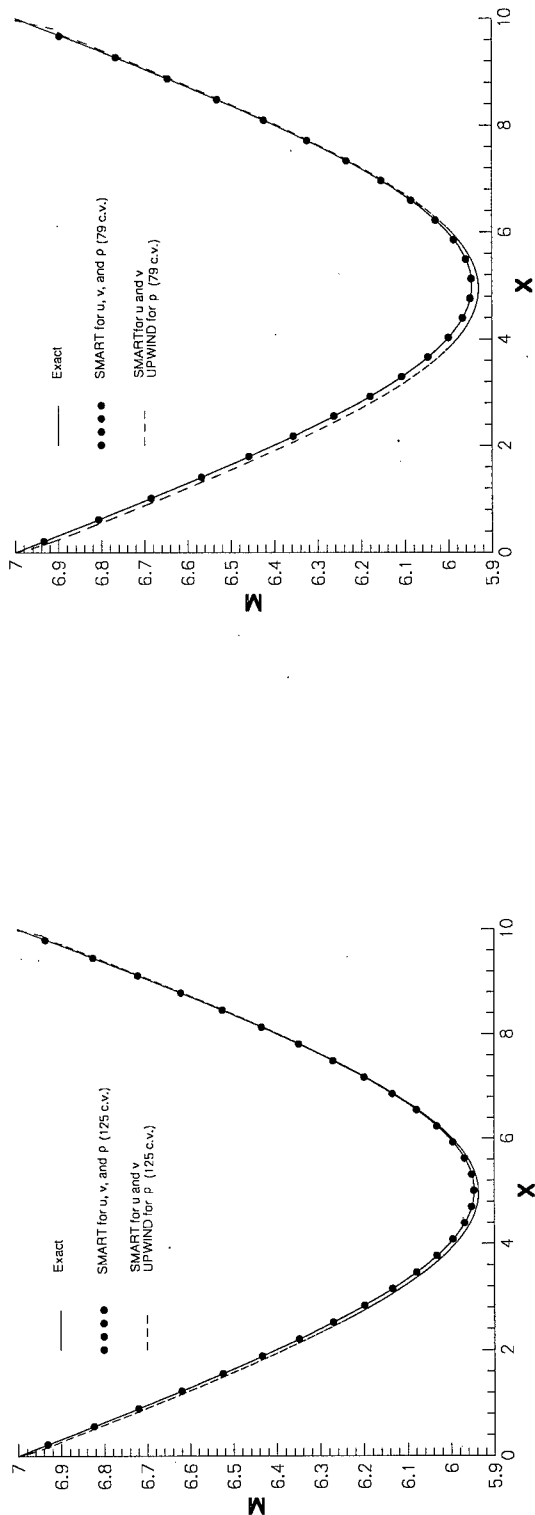


(c)

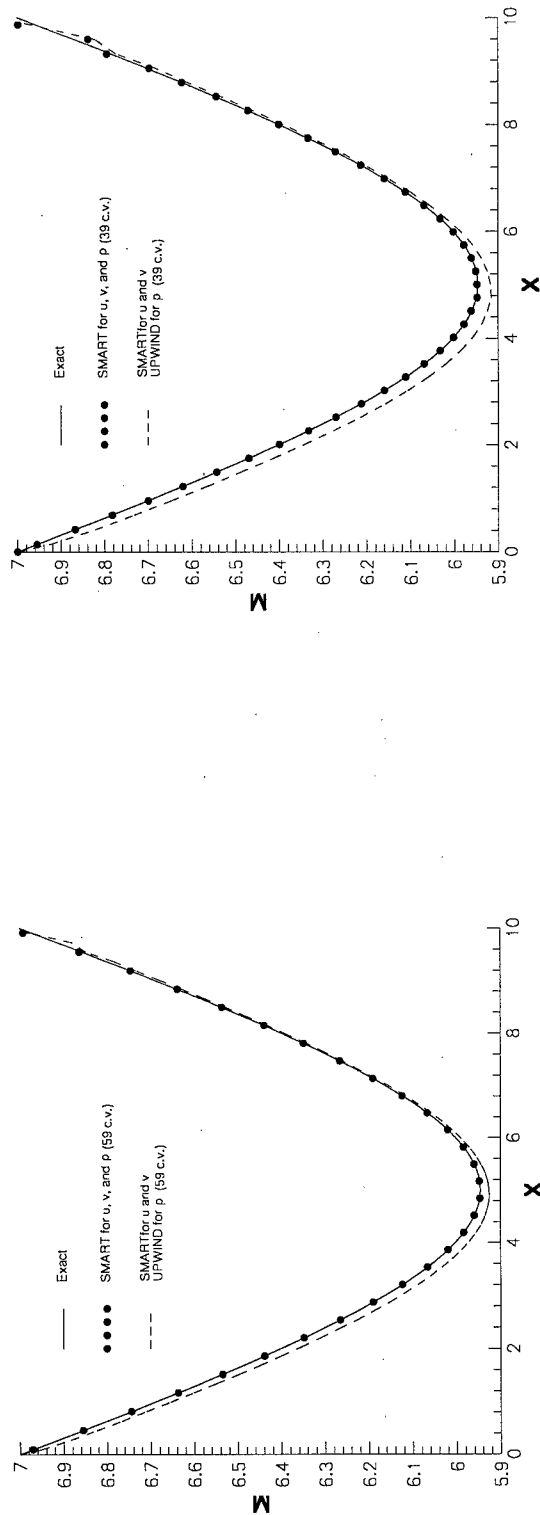


(d)

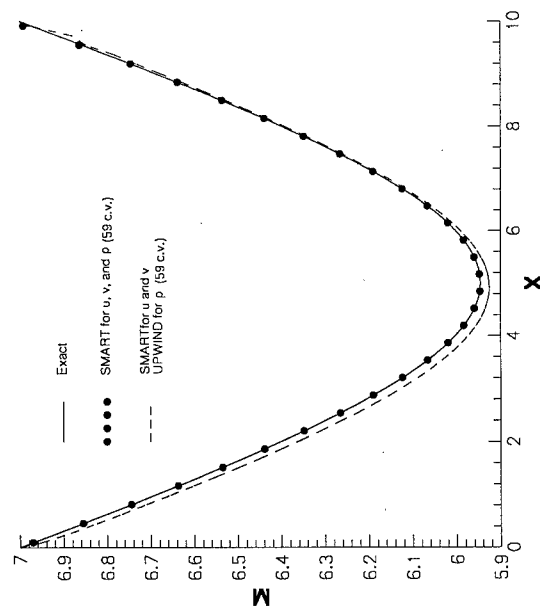
Fig. 5 Comparison of Mach number variation for an inlet Mach number of 0.3.



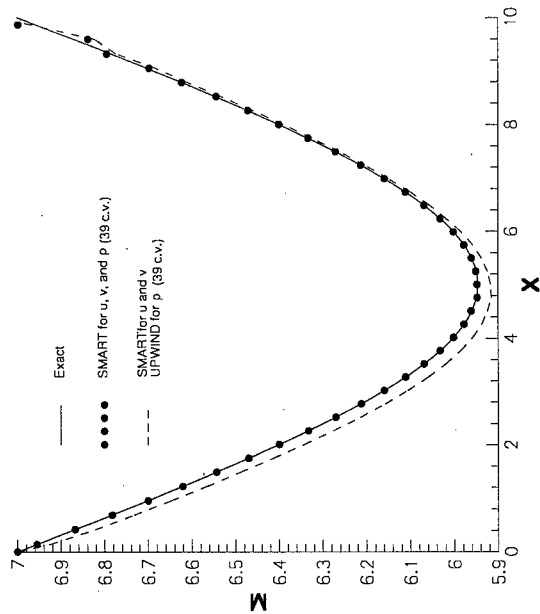
(a)



(b)

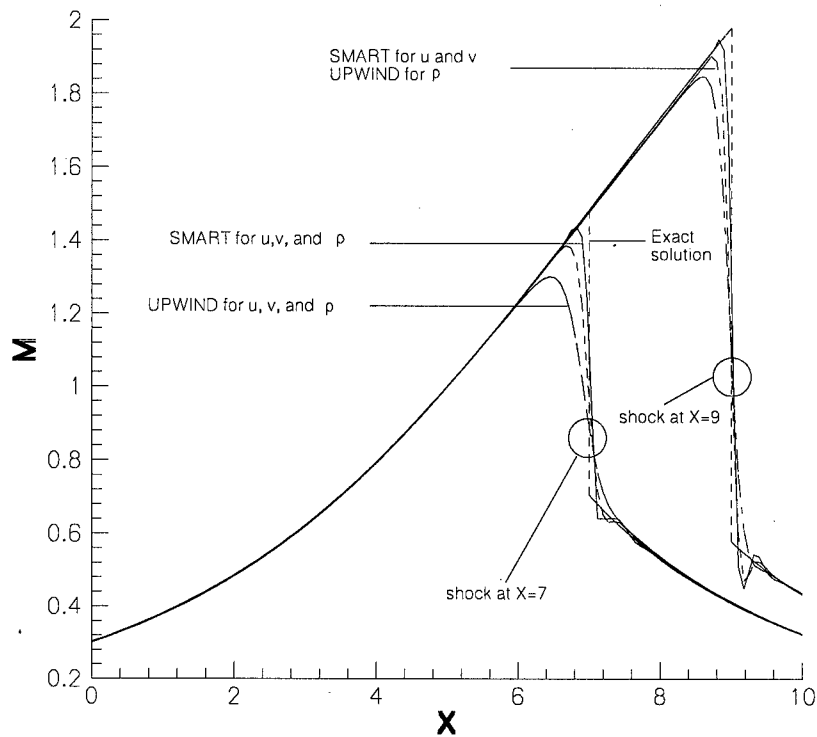


(c)

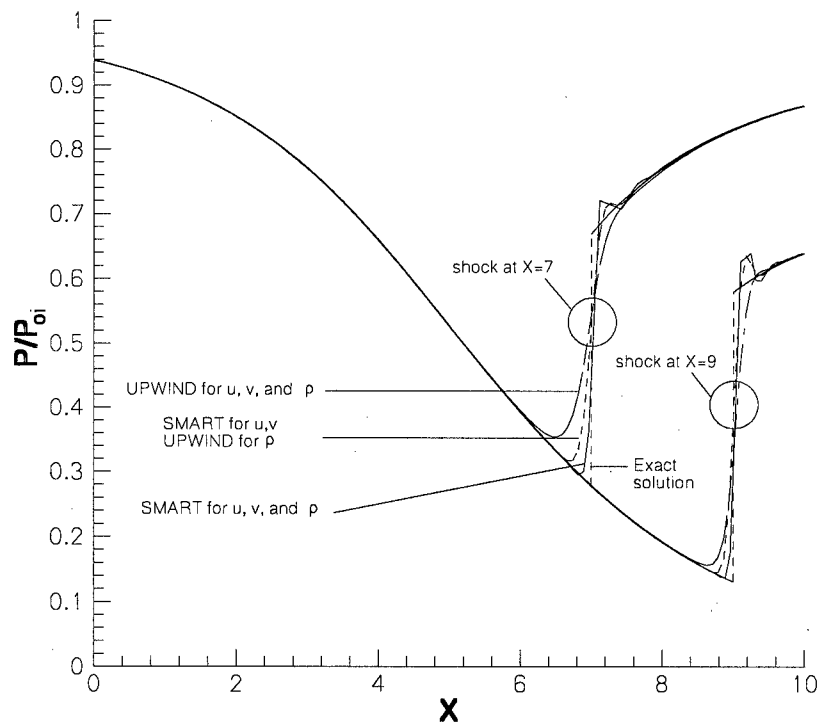


(d)

Fig. 6 Comparison of Mach number variation for an inlet Mach number of 7.

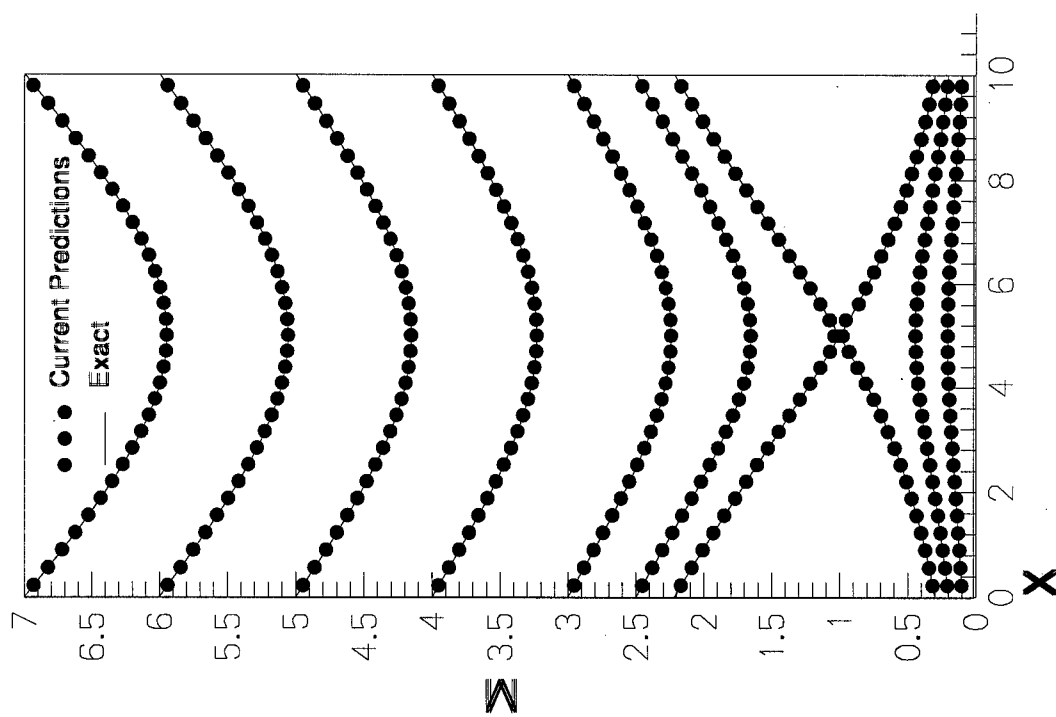


(a)

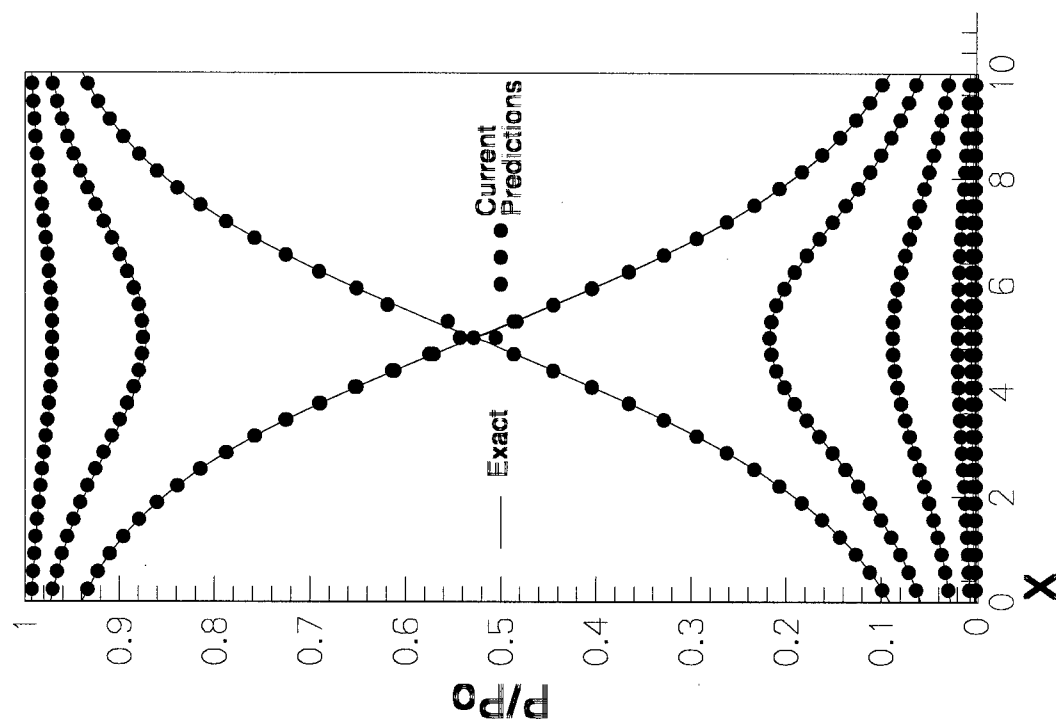


(b)

Fig. 7 Transonic inviscid flow in Laval nozzle: (a) Mach number distributions, (b) pressure distributions.

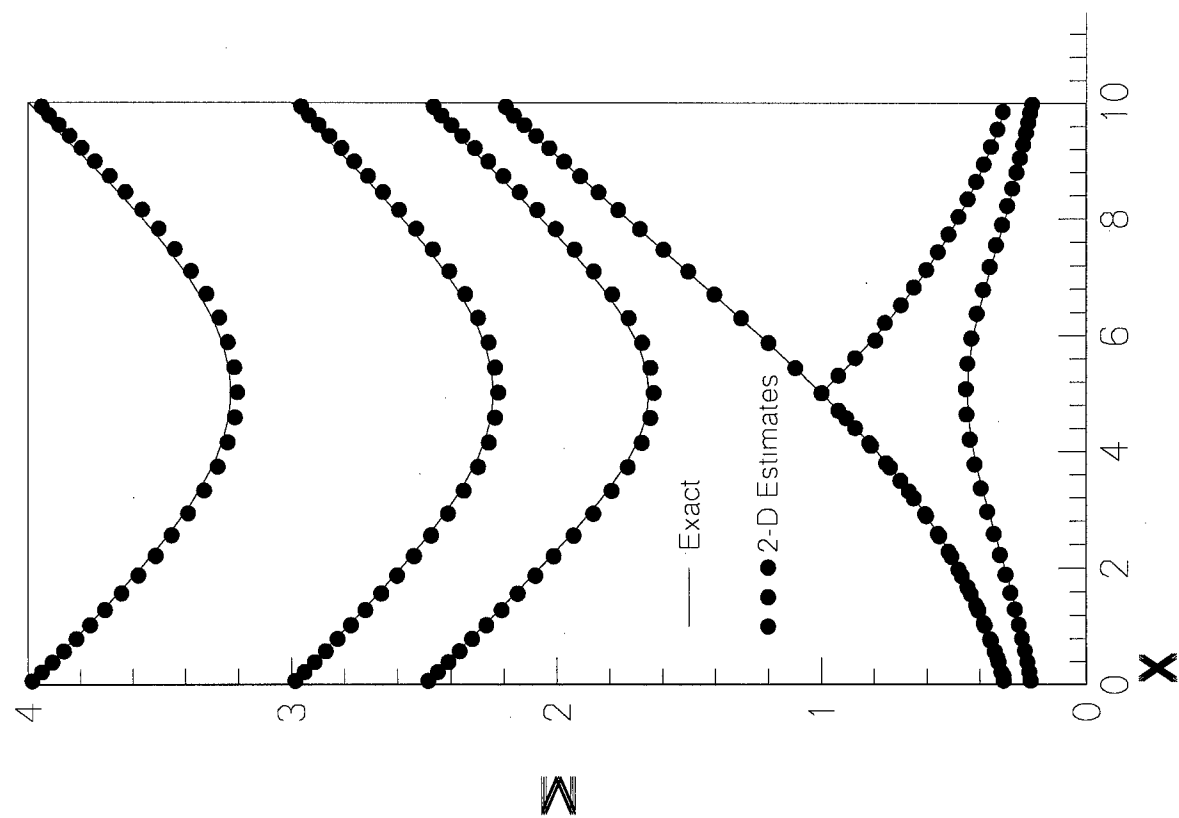


(a)

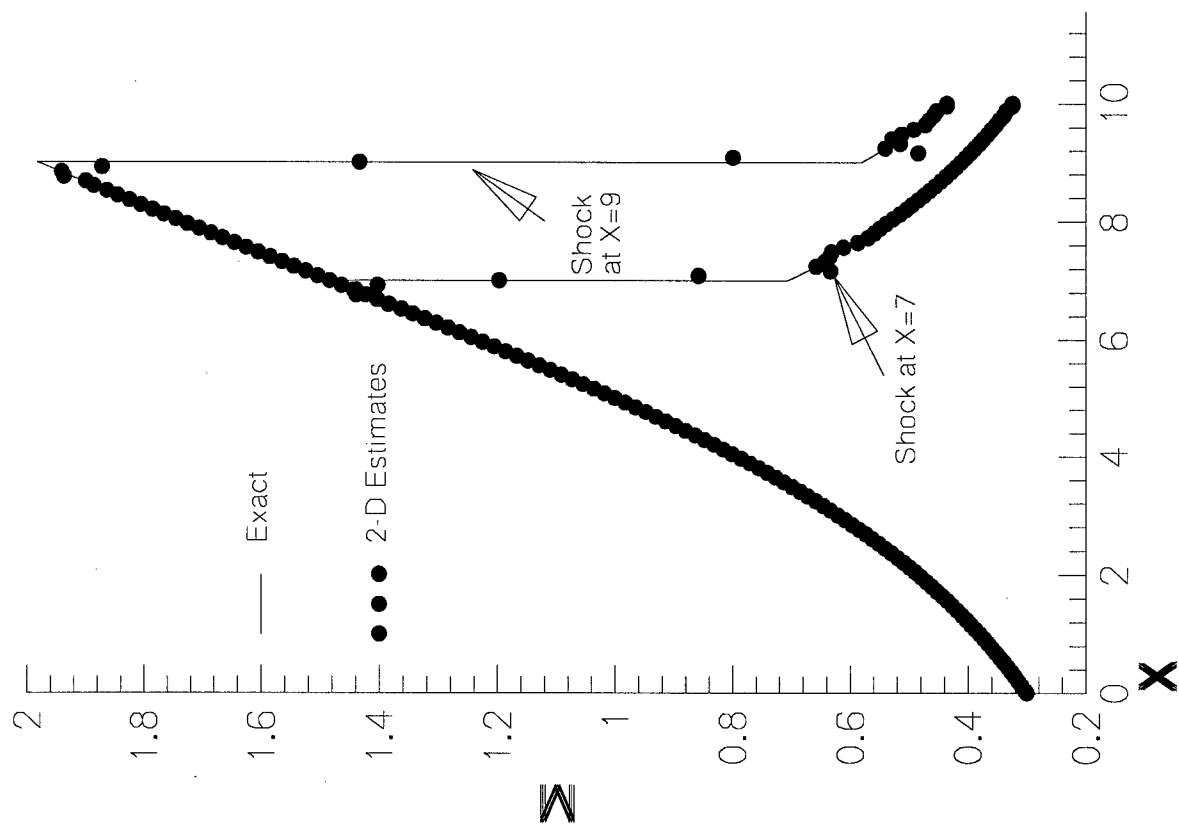


(b)

Fig. 8 Comparison of distributions of (a) Mach number and (b) pressure for one-dimensional inviscid nozzle flow.

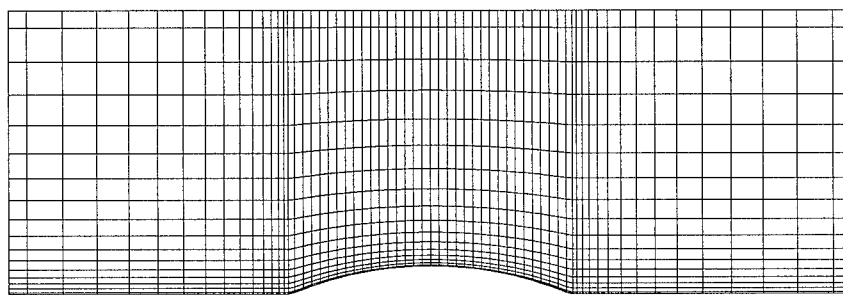


(a)

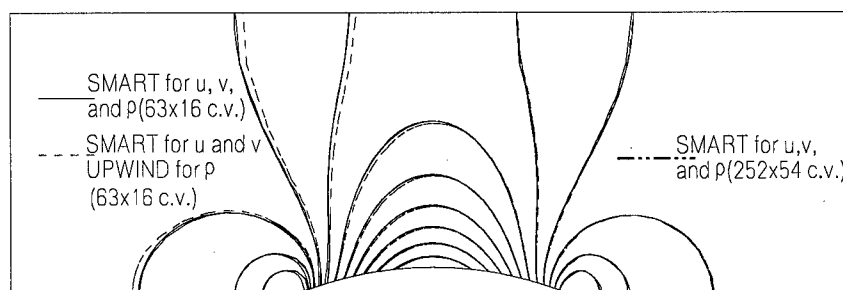


(b)

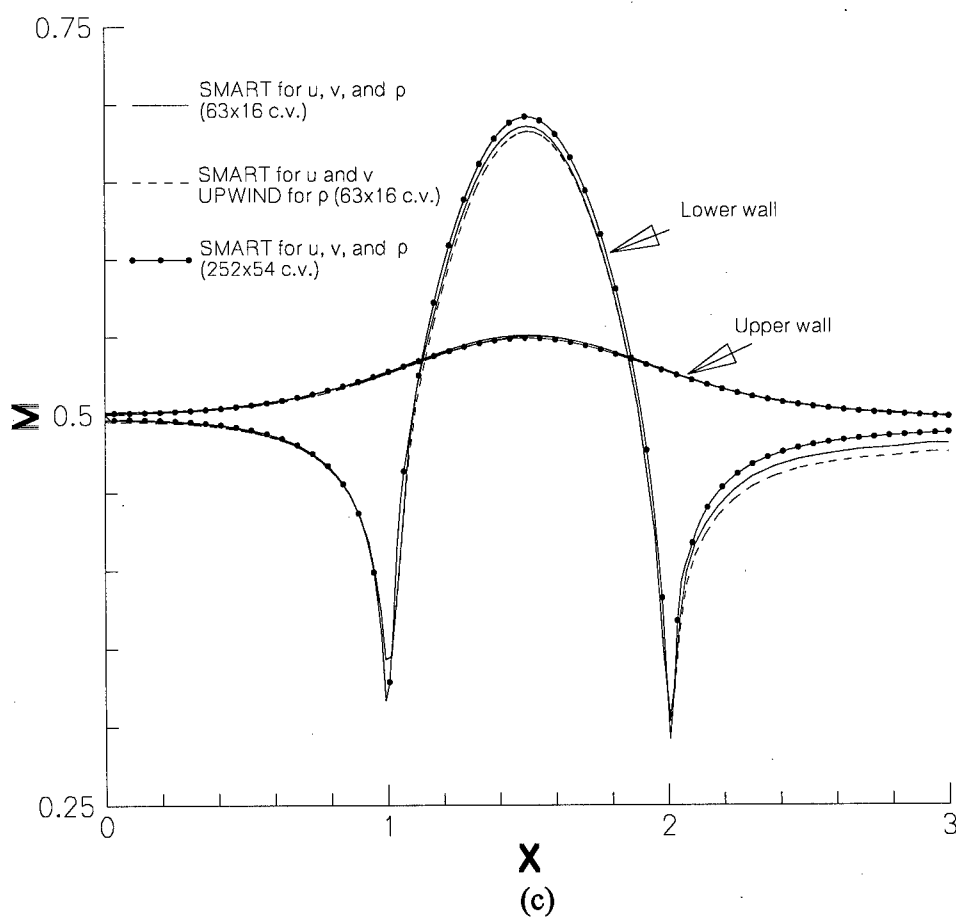
Fig. 9 Comparison of distributions of (a) area-averaged Mach number and (b) pressure for inviscid nozzle flow from 2-D solution.



(a)



(b)



(c)

Fig. 10 Subsonic flow over a 10% circular bump; (a) coarse grid used, (b) isobars, and (c) profiles along the walls.

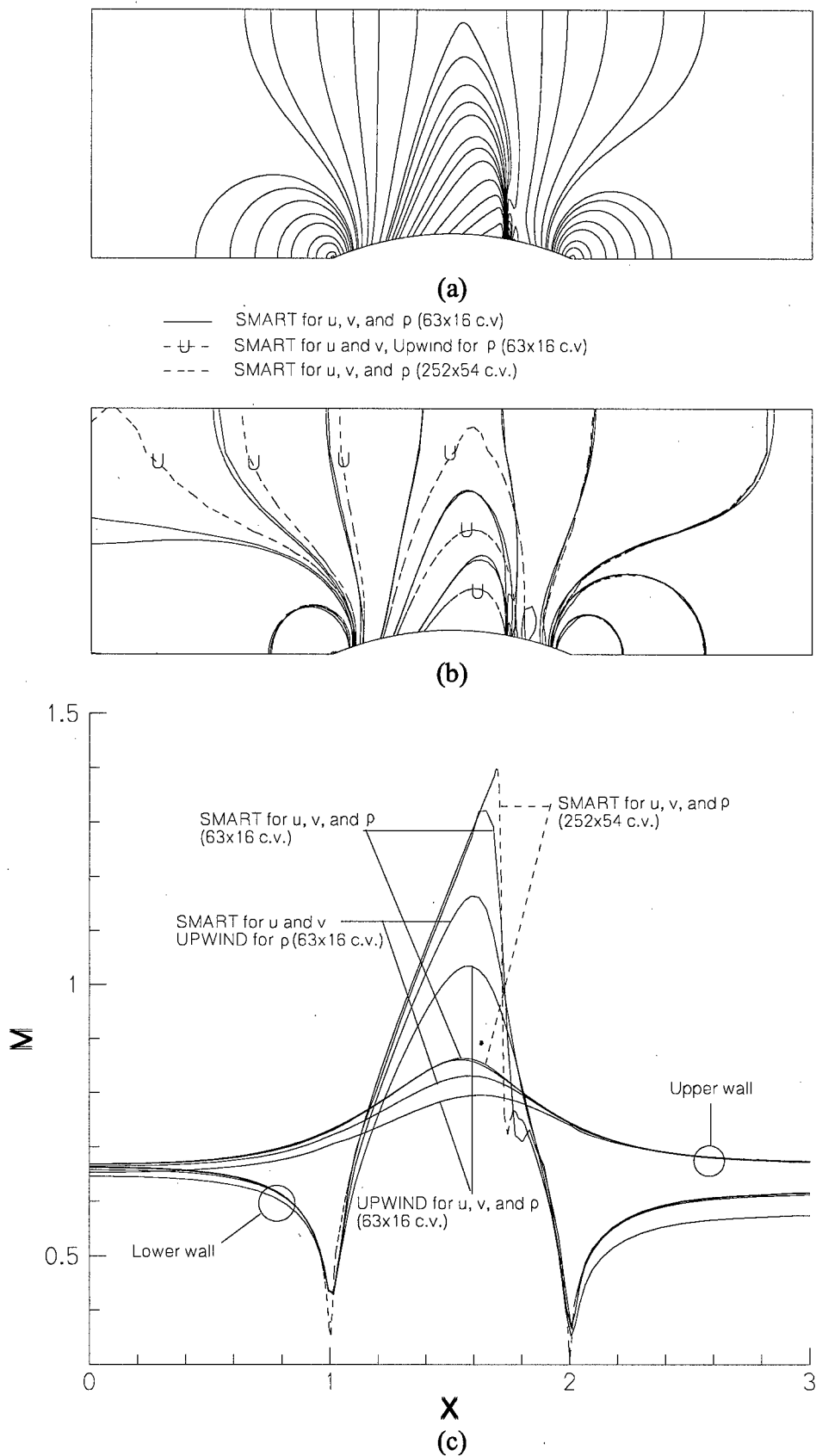


Fig. 11 Transonic flow over a 10% circular bump; (a) Isobars using a dense grid, (b) isobars using various schemes, and (c) profiles along the walls.

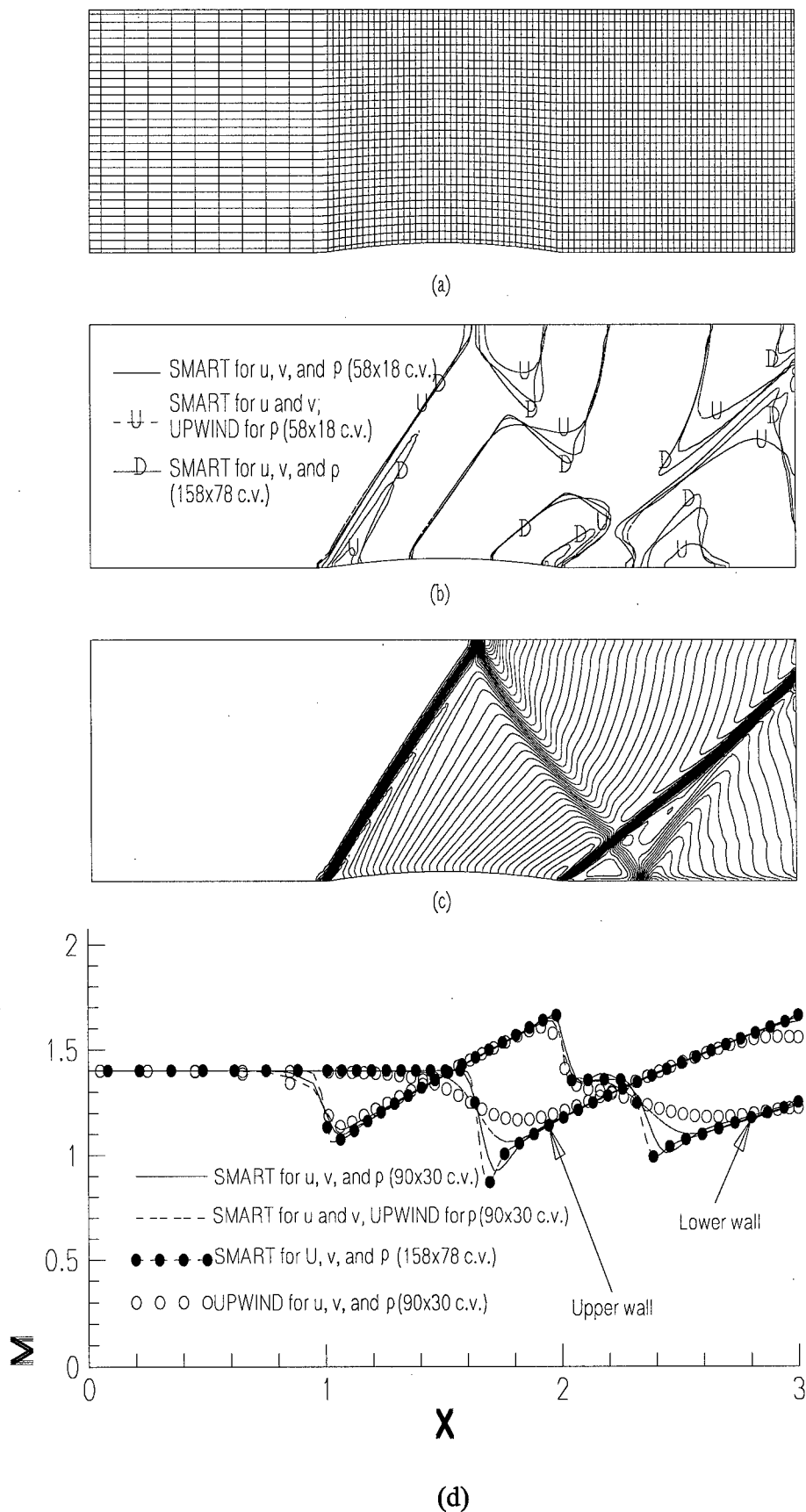


Fig. 12 Supersonic flow over a 4% circular bump ($M_{in}=1.4$); (a) coarse grid used, (b) Mach number contours using various schemes, (c) Mach number contours using a dense grid, and (d) profiles along the walls.

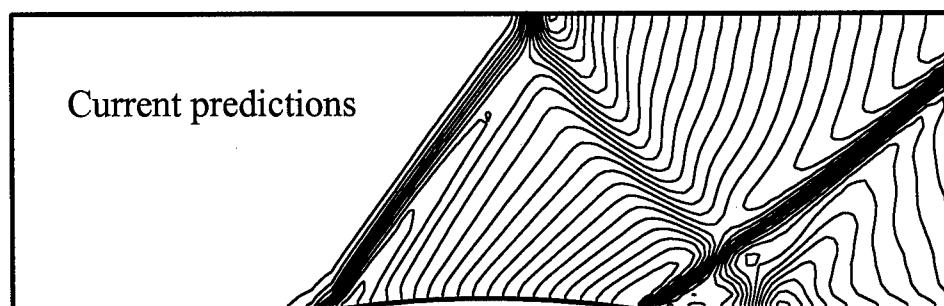
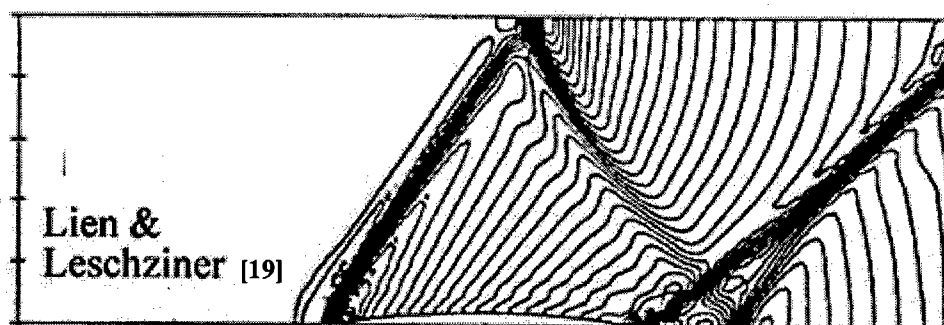
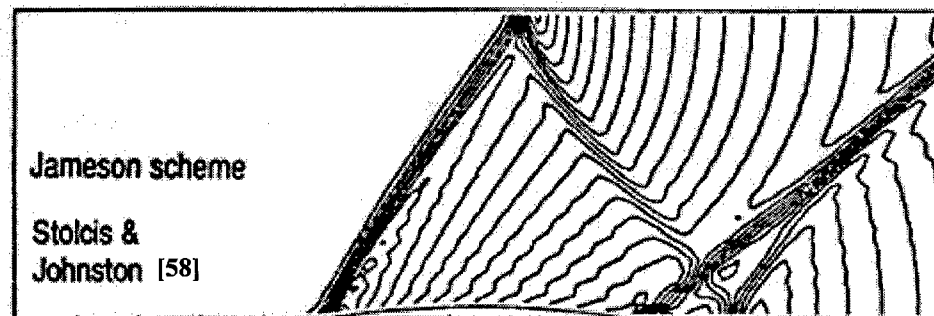
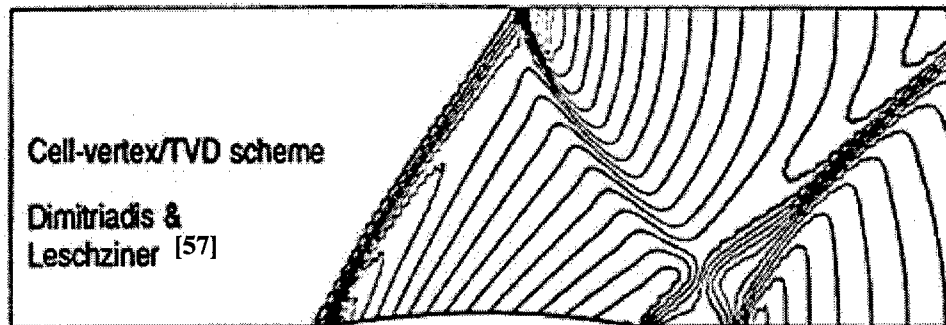
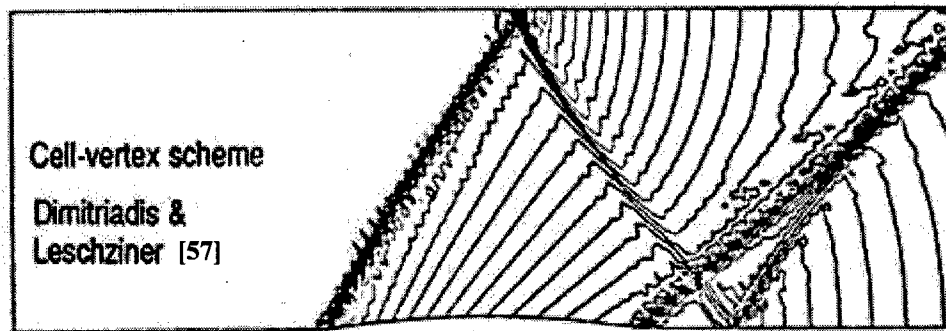


Fig. 13 Supersonic inviscid flow over 4% bump ($M_{in}=1.4$): Mach-number contours.

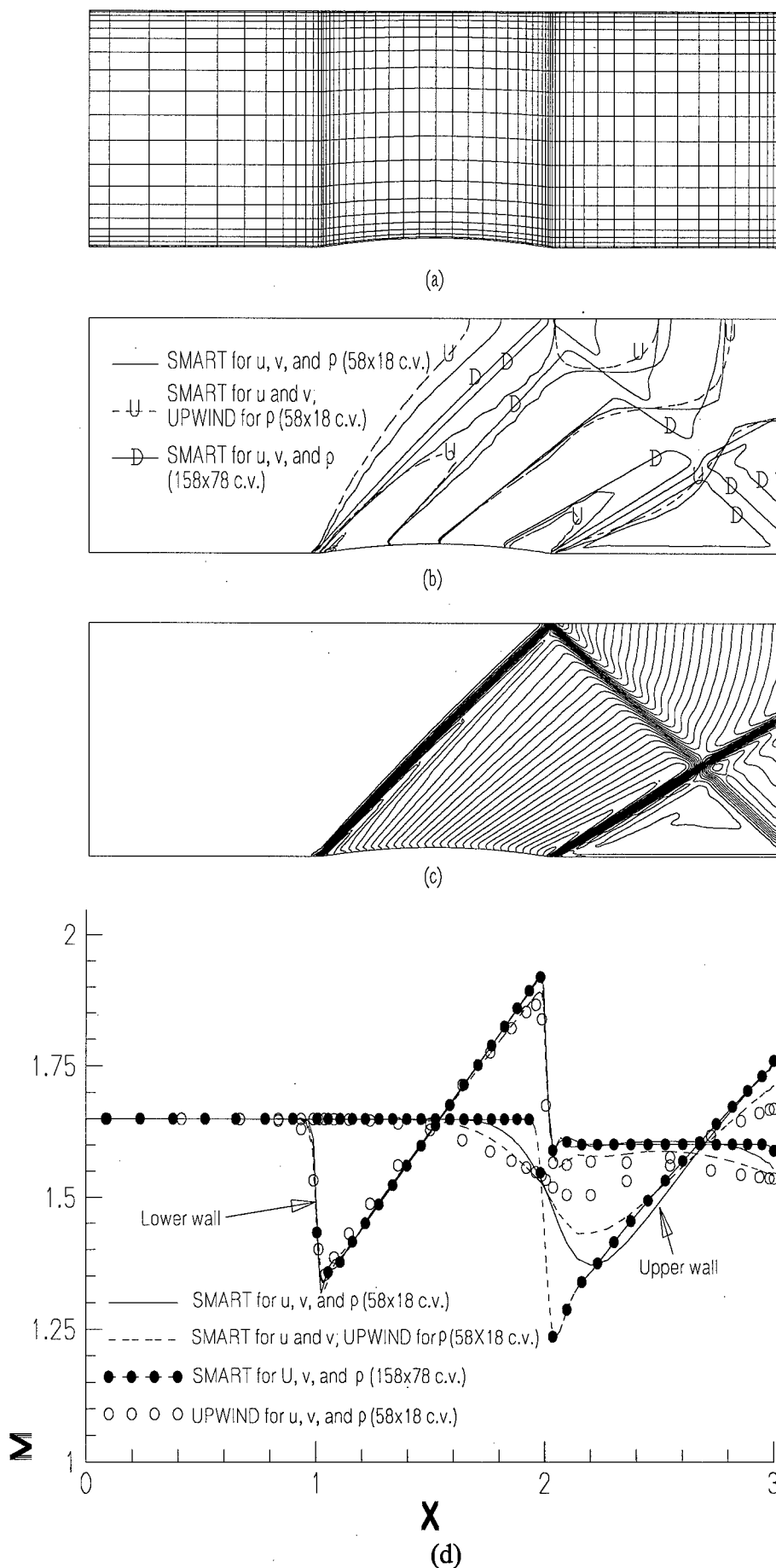
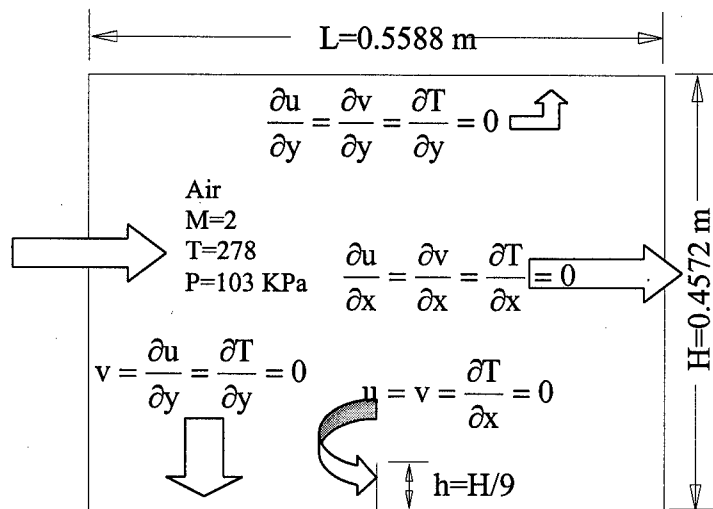
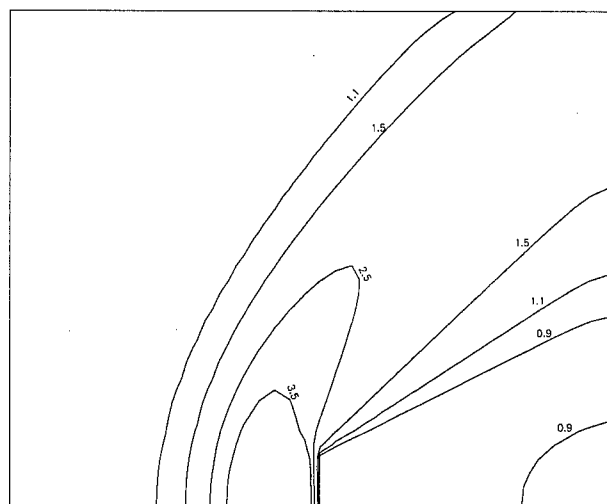


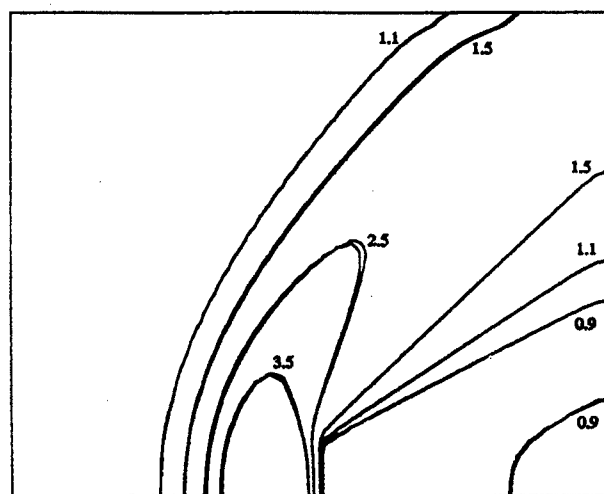
Fig. 14 Supersonic flow over a 4% circular bump ($M_{in}=1.65$); (a) coarse grid used, (b) Mach number contours using various schemes, (c) Mach number contours using a dense grid, and (d) profiles along the walls.



(a)

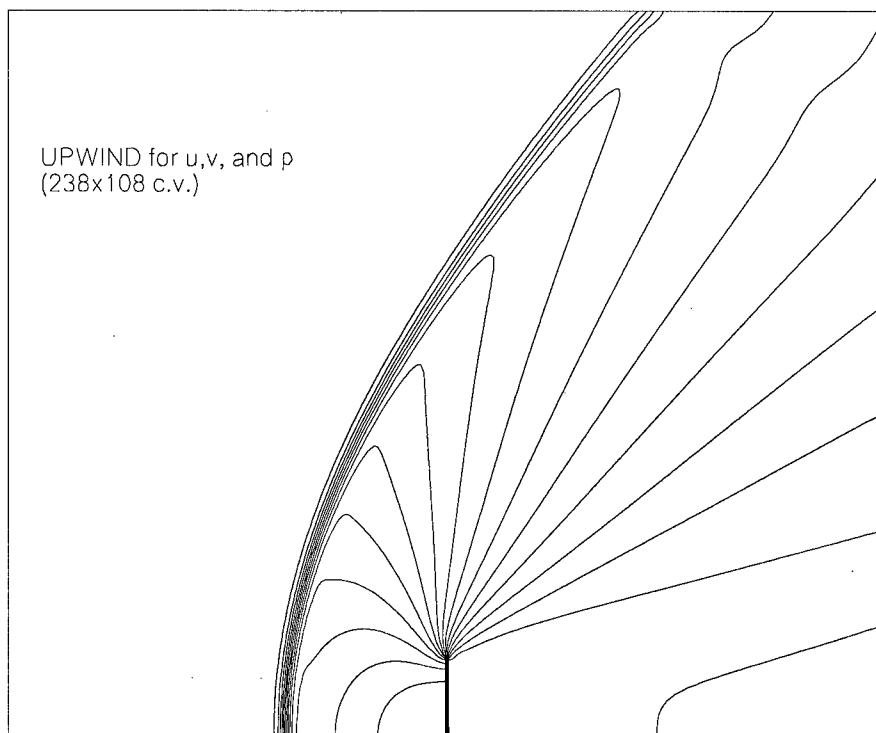


(b)

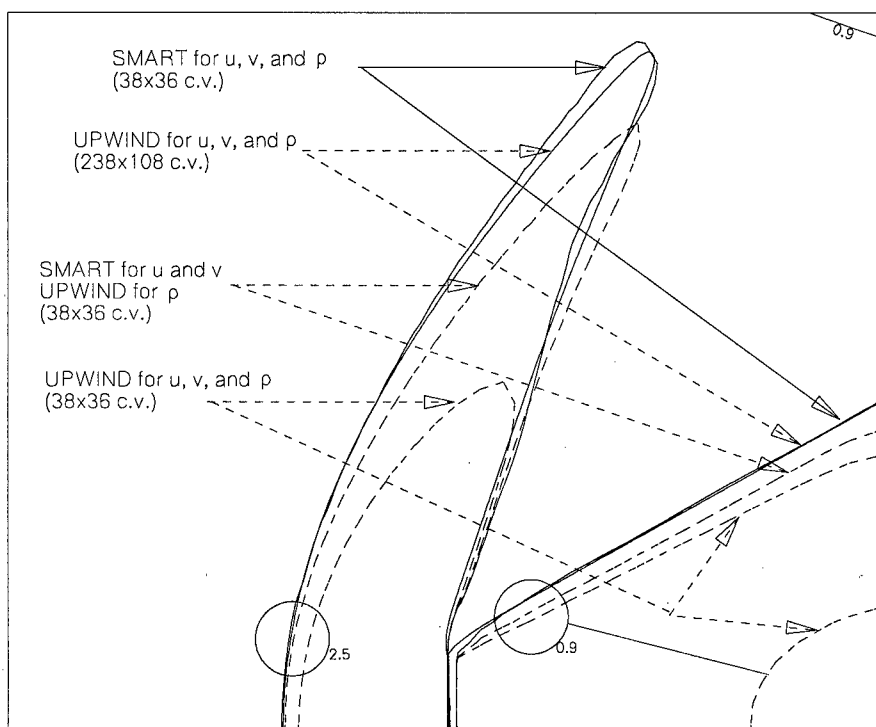


(c)

Fig. 15 Supersonic flow over an obstacle: (a) Physical situation, (b) Isobars using the upwind scheme (40X38 grid points), and (c) results obtained by Marchi and Maliska using (44x36 grid points).



(a)



(b)

Fig. 16 (a) Isobars generated using a dense grid; (b) Isobars generated using different schemes for supersonic flow over an obstacle.

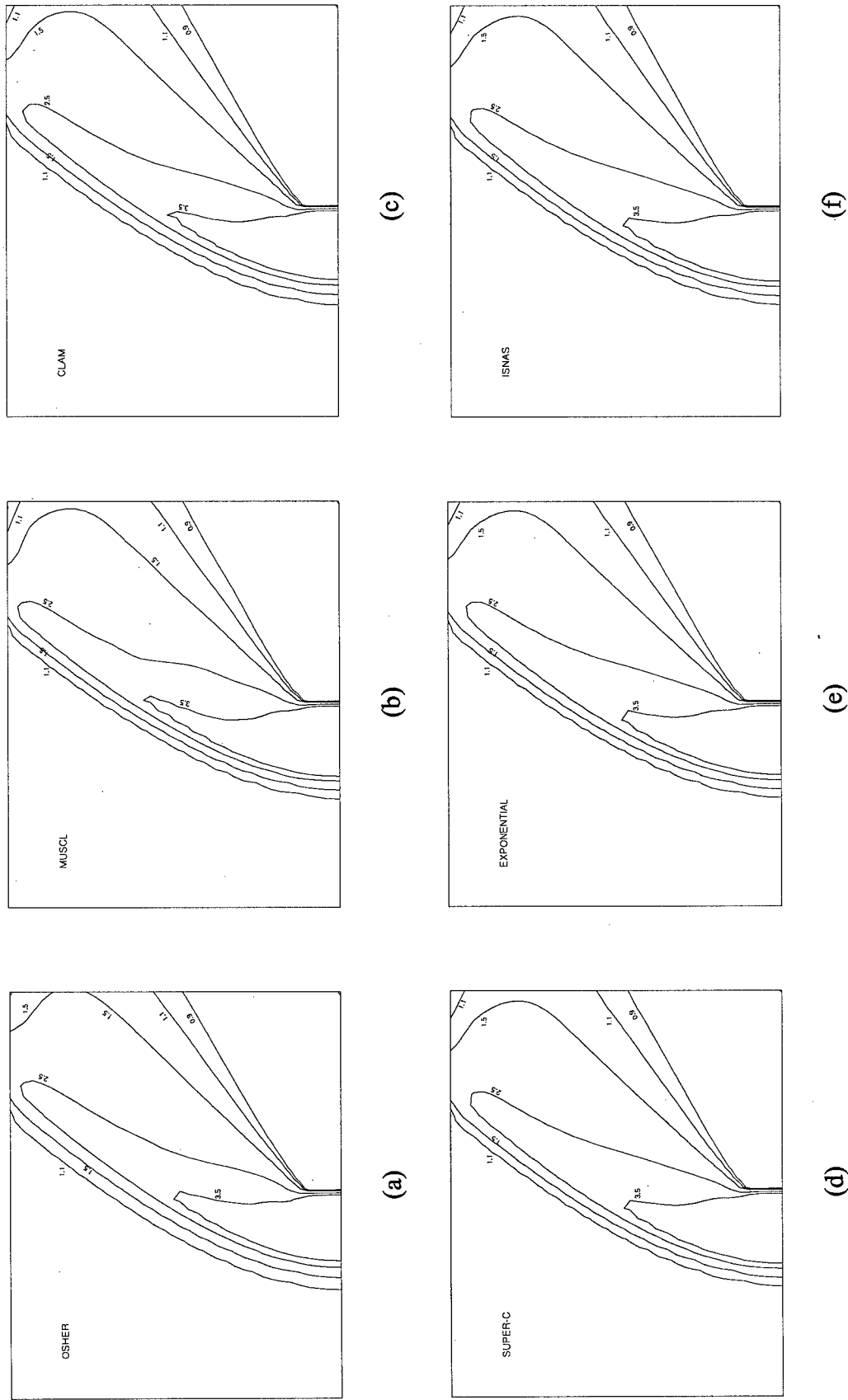


Fig. 17 Isobars for the flow over an obstacle obtained from different HR schemes.

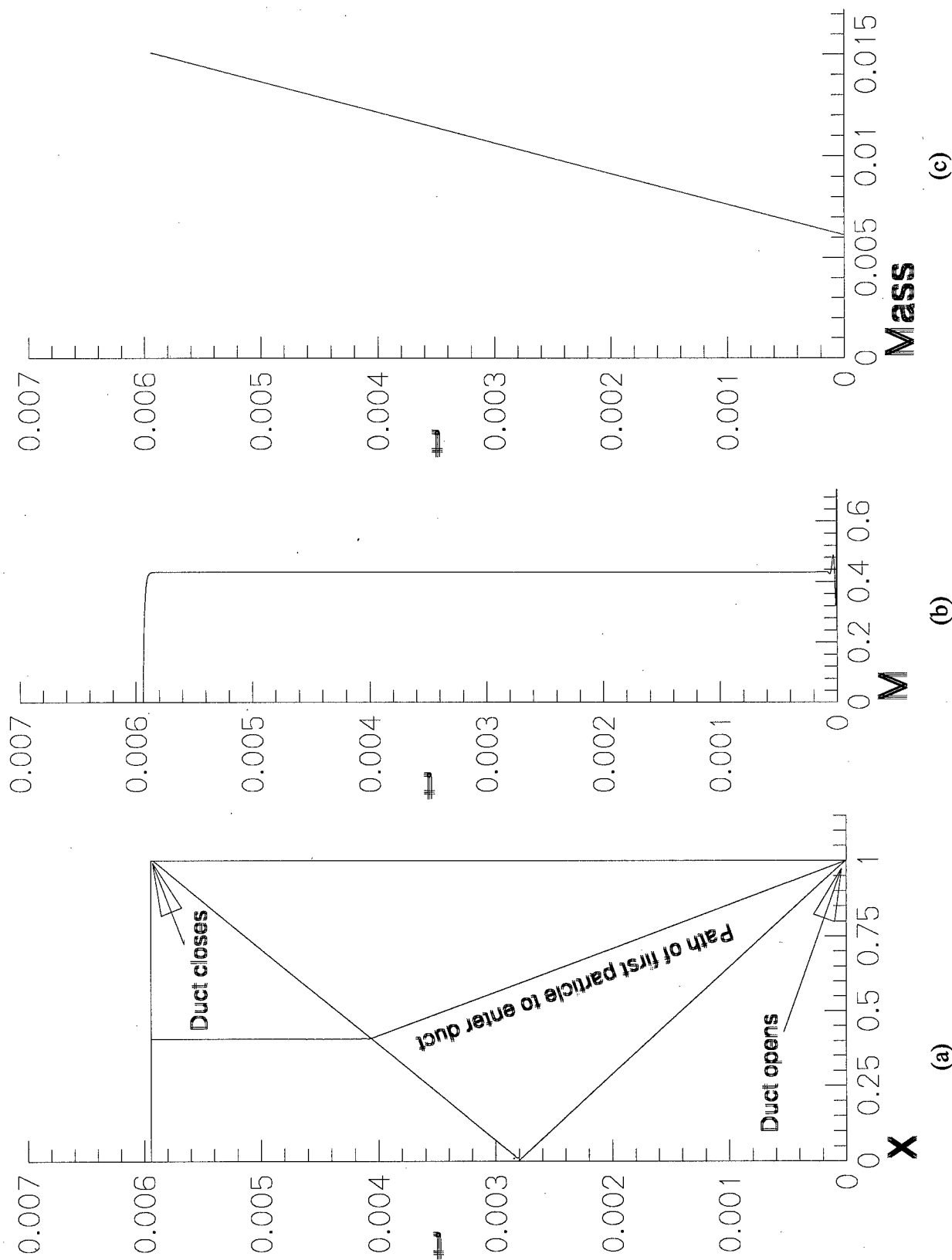


Fig. 18 (a) Wave diagram for optimum duct-filling process, (b) Mach number distribution at inflow; (c) Variation of mass with time.